Effect of Intermolecular Interactions on the Carbon 1s Near Edge X-ray Absorption Fine Structure (NEXAFS) Spectroscopy of *n*-Alkanes

A Thesis Submitted to the College of Graduate Studies and Research

in Partial Fulfillment of the Requirements for the

Degree of Master of Science

in the Department of Chemistry

University of Saskatchewan

Saskatoon

By

N.M. Sahan Daksitha Perera.

Permission to Use

In presenting this thesis in partial fulfillment of the requirements for a postgraduate degree from the University of Saskatchewan, I agree that the Libraries of this University may make it freely available for inspection. I further agree that permission for copying of this thesis in any manner, in whole or in part, for scholarly purposes may be granted by Professor S. G. Urquhart who supervised my thesis work or, in his absence, by the Head of the Department of Chemistry or the Dean of the College of Graduate Studies and Research. It is understood that any copying or publication or use of this thesis or parts thereof for financial gain shall not be allowed without my written permission. It is also understood that due recognition shall be given to me and to the University of Saskatchewan in any scholarly use that may be made of any material in my thesis. Request for permission to copy or to make other use of material in this thesis in whole or in part should be addressed to:

The Head

Department of Chemistry

University Of Saskatchewan

Saskatoon, Saskatchewan

Canada S7N 5C9

Abstract

"Matrix effects" in Near Edge X-ray Absorption Fine Structure (NEXAFS) spectroscopy are the spectroscopic changes induced by intermolecular interactions, providing sensitivity to local structure and order in solids and liquids. This project aims to identify the effect of intermolecular interactions caused by different *n*-alkane solid state structures on their NEXAFS spectra. Changes to the carbon 1s NEXAFS spectra are studied as a function of their solid state structure and organization. Two experimental approaches were proposed in this project. In the first approach, different *n*-alkane crystal structures (orthorhombic, monoclinic, etc.) are examined which arise as a function of *n*-alkane chain length. In the second approach, changes observed through the pre-melting point order-disorder phase transition found in *n*-alkanes are examined. This work will explore the characteristic spectroscopic differences observed between *n*-alkanes in different crystalline forms as well as in the disordered phase below the melting points.

In this project, well-ordered diamond shape *n*-alkane single crystals were obtained by solution casting, using experimental conditions optimized for each *n*-alkane. As circularly polarized radiation will average the effect of molecular orientation, circularly polarized radiation was used to obtain the NEXAFS spectra of *n*-alkanes. However, in the analysis of the NEXAFS spectra of *n*-alkanes recorded with the left circularly polarized X-rays, a significant linear polarization contamination was found. Therefore, linearly polarized X-rays were used to acquire angle dependent NEXAFS spectra, where the X-ray polarization was deliberately aligned along the principal axes (X, Y) of the *n*-alkane crystal.

It was observed that the room temperature carbon 1s NEXAFS spectrum of *n*-octacosane ($C_{28}H_{58}$) was different from that of the other *n*-alkanes, *n*-tetracosane ($C_{24}H_{50}$), *n*-tricosane ($C_{23}H_{48}$) and *n*-tetracontane ($C_{40}H_{82}$). This difference can be attributed due to the different crystal

packing of *n*-octacosane ($C_{28}H_{58}$ - monoclinic) relative to the other *n*-alkanes (triclinic and orthorhombic), suggesting different intermolecular interactions (matrix effects) in *n*-octacosane ($C_{28}H_{58}$).

The analysis of the temperature dependent NEXAFS spectra of *n*-alkanes reveals that samples of the short chain *n*-alkane crystals, specially *n*-tricosane ($C_{23}H_{48}$), *n*-tetracosane ($C_{24}H_{50}$) and *n*-octacosane ($C_{28}H_{58}$), sublimed in the STXM microscope. Changes observed in the carbon 1s NEXAFS spectra of *n*-tetracontane ($C_{40}H_{82}$) with temperature were attributed to the order-disorder transition. This further illustrates the existence of matrix effects in the NEXAFS spectra of *n*-alkanes.

Acknowledgements

First of all, I would like to thank to my supervisor, Professor Stephen G. Urquhart, for his endless support, exceptional guidance and faith in me throughout this project. He gave me the opportunity to do this wonderful advanced synchrotron based work. The experience which I gained throughout this project will surely fill my research career in colours.

I would like to thank to the member of my Advisory Committee Professor Robert Scott and Advisory Committee Chair Professor Marek Majewski for their advice during the program.

I am grateful to the members of the Professor Urquhart lab: Mitra Masnadi, Amara Zuhaib, Shaylin Eger, Shirin Behyan, Heba Fraij and Dr Wei Cao for their wonderful support during this program.

I wish to thank the Department of Chemistry, University of Saskatchewan and Canadian Light Source which are supported by NSERC, NRC, CIHR, and the Province of Saskatchewan, for providing more advance experimental source throughout this project.

Special thanks go to the Garth Parry for his help with the STXM heating cell.

Further I would like to thank Soft X-ray microscopy (SM) beam line scientist in the Canadian Light Source, Dr Jian Wang, for his endless support throughout this project.

Finally I would like to express my deepest gratitude to my family, brother, sister in-law, parents, girlfriend and her family for their encouragement and faith on me.

Table of Contents

List of Tables

List of Figures

Chapter 1

Chapter 2

Chapter 3

List of Abbreviations

BM	Bending Magnets
CLS	Canadian Light Source
DFT	Density Functional Theory
DSC	Differential Scanning Calorimeter
EELS	Electron Energy Loss Spectroscopy
EMR	Electro Magnetic Radiation
EPU	Elliptically Polarized Undulator
FWHM	Full-Width Half Maximum
ID	Insertion Device
IPA	isopropyl alcohol
LCP	Left Circular polarization
LD	Linear Dichroism
LUMO	Lowest Unoccupied Molecular Orbital
MO	Molecular Orbital
NEXAFS	Near Edge X-ray Absorption Fine Structure
OD	Optical Density
OM	Optical Microscope

OSA	Order Sorting Aperture
PET	Poly(ethylene terephthalate)
PEO	Poly(ethylene oxide)
PIB	Poly(isobutylene)
PID	Proportional Integral Derivative
PP	Poly(propylene)
PPO	Poly(propylene oxide)
RCP	Right Circular Polarization
RTD	Resistance Temperature Device
SM	Spectromicroscopy
STXM	Scanning Transmission X-ray Microscope
TDM	Transmission Dipole Moment
ZP	Zone Plate

1. Introduction

1.1 Near Edge X-ray Absorption Fine Structure Spectroscopy (NEXAFS)

NEXAFS spectroscopy measures the photoabsorption cross section associated with the excitation or emission of a core electron following the absorption of an X-ray.[1-6] Generally, the X-ray absorption cross-section decreases with increasing photon energy. However, at discrete photon energies which are specific for the type of absorbing atoms, a sudden increase in the absorption cross section area is observed. This is known as the absorption edge. These absorption edges are element specific as each element has a characteristic core binding energy, such as carbon 1s:~ 284 eV, nitrogen 1s: ~ 409 eV and oxygen 1s: ~ 543 eV.

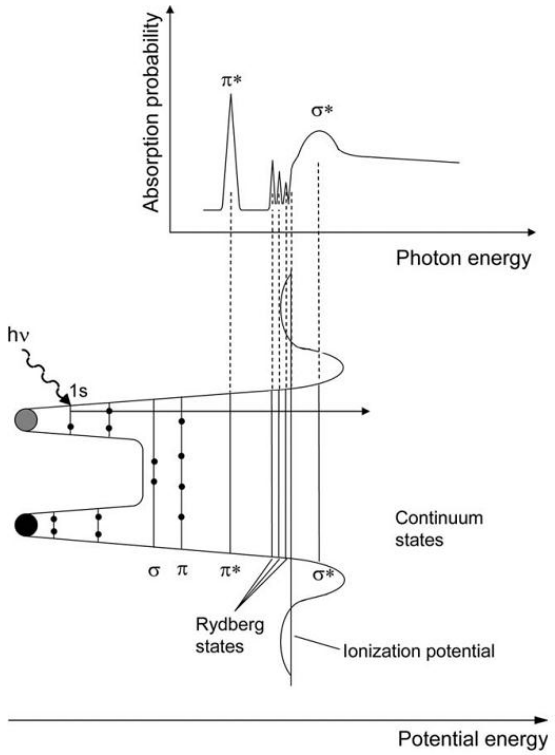

Figure 1.1 Schematic diagram of the NEXAFS process in a diatomic molecule XY (figure reprinted from Hähner *et al.*[5] with permission).

A NEXAFS spectrum ranges usually from few electron volts (eV) below the photoionization threshold up to few tens of eV above. The schematic diagram of the NEXAFS process is shown in **Figure 1.1**. When an incoming X-ray of sufficient energy is absorbed, a core (1s) electron can be excited into the continuum, into unoccupied π*, Rydberg and σ* core excited states. Rydberg transitions are atomic-like features in core excited molecules, such as carbon 1s → 3s, carbon 1s → 3p transitions. These Rydberg peaks are usually sharp, but weak in intensity and appear below the ionization potential. Usually, core → π*, Rydberg and σ* transitions can be differentiated by their energy position and the shape of the corresponding feature.

Regarding the shape, the width of a resonance is determined by the resolution of the monochromator, the lifetime of the core excited state, and molecular vibrations. Generally, core → π* transitions are sharper than core → σ* transitions. The reason for the broadening of the core → σ* transitions is the increased probability of decay to the continuum state and large overlap of these states with the continuum states. Carbon 1s → π* transitions are not usually in the continuum.[1,2,5,7] and usually appear lower in energy with respect to the core → σ* transitions.

Core excitation transitions in molecules are generally considered to follow an "atomic propensity rule". According to this rule, excitations follow the atomic selection rule ($\Delta l = \pm 1$) on the core excited atom as the spin quantum number of photon is 1. This is not a precise rule as the orbital angular momentum is not well defined in complex molecules. For second row atoms, the electric-dipole matrix element for 1s core excitation is dominated by terms involving 1s atomic orbitals of the initial state and the 2p atomic orbitals localized at the site of the localized core excitation.[8] Therefore, for excitation from a 1s orbital, the transition dipole moment (TDM) points in the same direction as the p-component in the unoccupied molecular orbital on the core

excited atom.[9] Furthermore, the intensity of the allowed transitions mainly depends on the angle between the direction of the electric field vector of the X-ray and the direction of the transition dipole moment. The transition obtained has the maximum intensity if the two vectors are parallel to each other, and minimum if they are normal to each other.[1,4,5,9-11]

X-ray absorption leads to decay processes. In order to acquire the spectra presented in **Figure 1.1**, transmission of the photons through the sample, or the fluorescent photons or the electrons emitted by the sample should be converted into a detectable signal. Therefore absorption can be measured either by transmission or by measuring the decay processes.

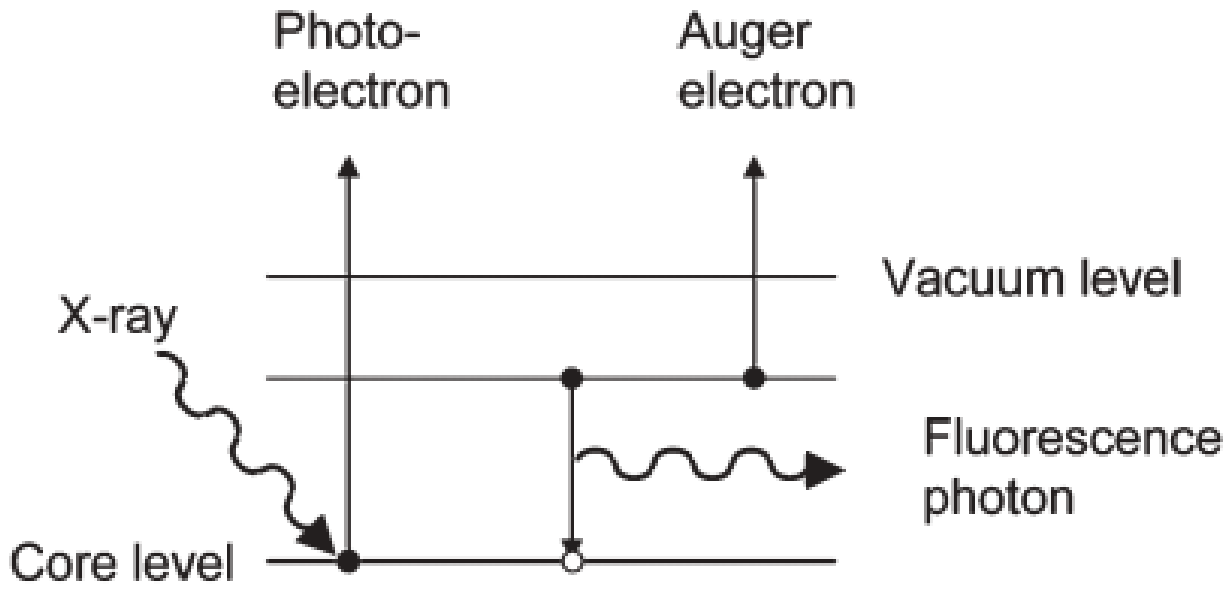

Figure 1.2 Schematic energy diagram of the X-ray absorption and core hole decay processes (figure reprinted from Chen *et al.*[6] with permission).

Figure 1.2 shows the possible decay processes (Auger electron and fluorescent photon) following the excitation or ionization of a core electron. X-ray absorption can cause valence ionization as well, which would not lead to those decay pathways. According to **Figure 1.2**, a core hole is generated due to the photoionization of a core electron upon X-ray absorption. As a

result of this process, it will create short lifetime core excited states which leads to a series of relaxation processes. Auger emission occurs when a less tightly bound electron refills the core hole, and the excess energy is taken away by the ejection of an Auger electron. The fluorescent photon will be produced when an electron refills a core hole and the excess energy is carried away. The NEXAFS spectrum can be formed by measuring the amount of emitted photons or electrons as a function of incident photon energy.

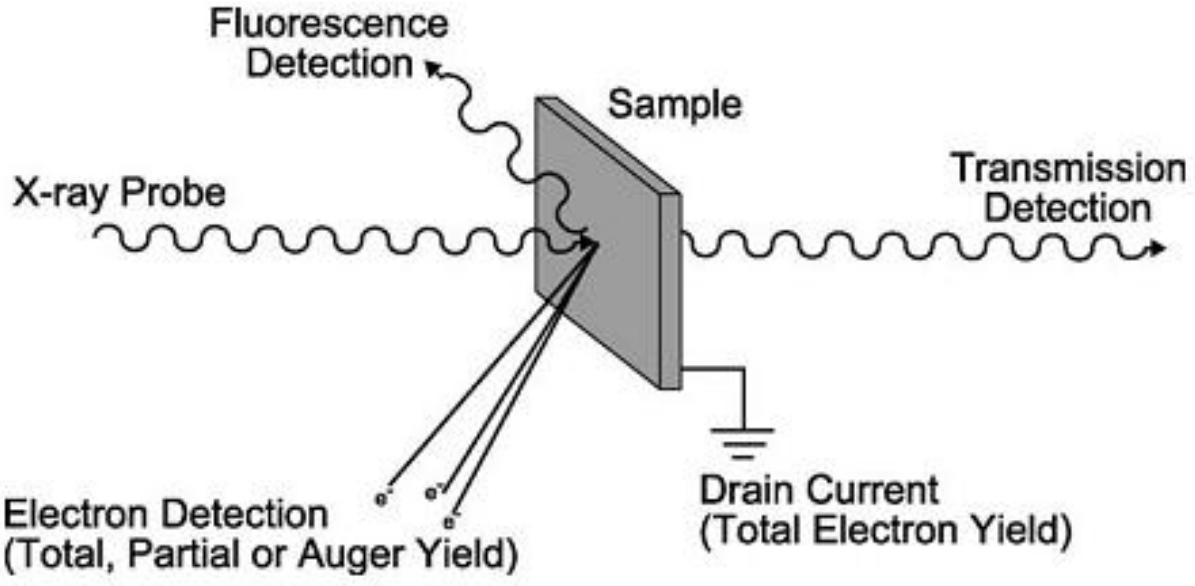

Figure 1.3 Schematic of the possible measurements techniques for NEXAFS spectroscopy (figure reprinted from Watts *et al.*[7] with permission).

Figure 1.3 shows the three detection modes used for NEXAFS spectroscopy: electron yield, fluorescent yield and the direct measurement of photon transmission through the sample. Partial and total electron yield indirect measure the NEXAFS spectra through the detection of photoemitted electrons. In partial electron yield, only a certain kinetic energy range of the emitted electrons are detected. In sample current total electron yield mode, the drain current

produced from all emitted electrons are measured, which corresponds to all primary and secondary photoelectrons.

In this project, as long as moderately thin *n*-alkane crystals are used, transmission measurements could be used. This also allows single crystals to be observed in the STXM microscope.

The Beer-Lambert law can be used to convert the photon transmission to optical density according to

$$OD = -\ln (I/I_0) \quad (1.1)$$

Where for a given X-ray energy, I_0 is the incident flux of the X-ray beam, I is the transmitted flux through the sample and ln is the natural logarithm.[12] Further, the OD is related to the sample properties by:

$$OD = \mu.\rho.t = \mu_1 t \quad (1.2)$$

Where μ (cm^2/g) is the mass absorption coefficient, ρ (g/cm^3) is the density of the material, t (cm) is the sample thickness and $\mu_1(cm^{-1}) = \mu\rho$ is the linear absorption coefficient. Thomas *et al.*[12] showed that the mass absorption coefficient is the function of the atomic absorption cross section σ_a (cm^2) and atomic mass A (g/mol) according to

$$\mu = (N_a/A)\times\sigma \quad (1.3)$$

Where N_a is the Avogadro number.

Therefore, from the direct measurement of the X-ray transmission, it is possible to calculate optical density. NEXAFS spectra are presented as optical density versus photon energy.

1.1.1 Chemical Analysis by NEXAFS Spectroscopy

This section will explain the major characteristics of the NEXAFS spectroscopy of organic molecules, in particular the chemical sensitivity towards different functional groups in a molecule. Various functional groups within a molecule can be chemically differentiated by NEXAFS spectroscopy. The differentiation of different functional groups within the molecule can be illustrated by the example of the carbon 1s NEXAFS spectrum of poly(styrene-*r*-acronitrile) shown in **Figure 1.4**.

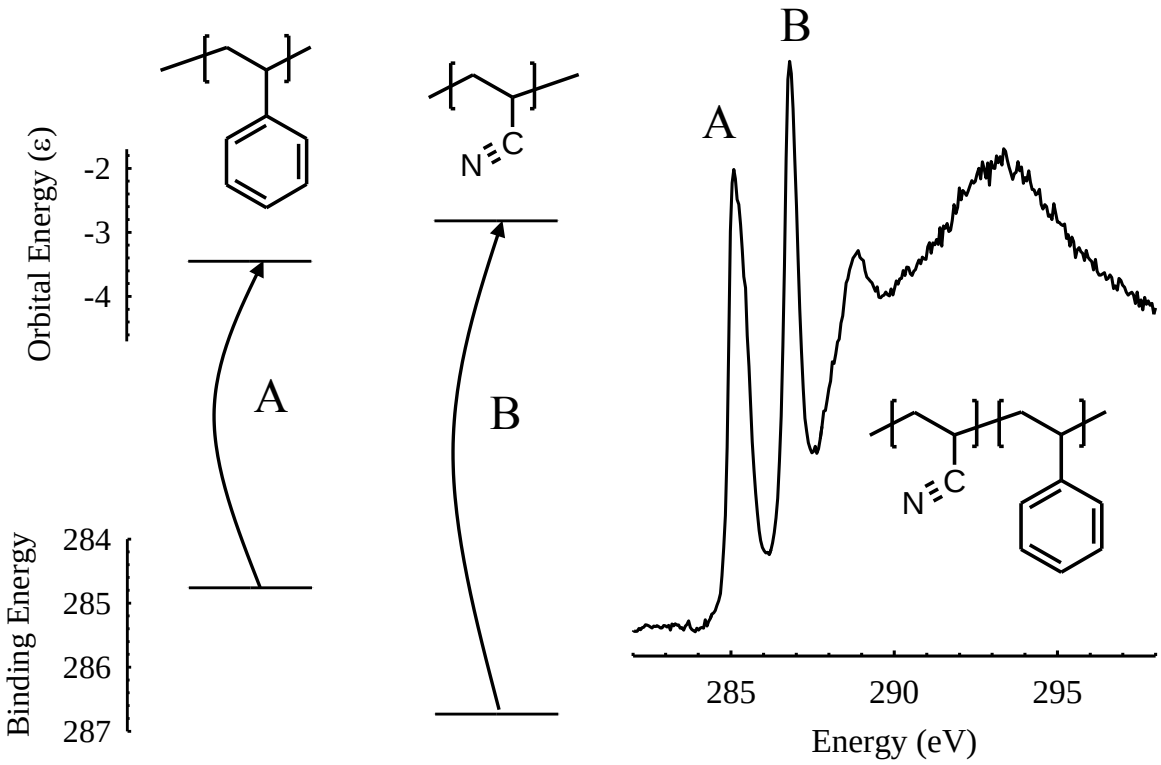

Figure 1.4 Schematic for the carbon 1s NEXAFS spectrum of poly(styrene-*r*-acronitrile) (figure reprinted from Ade *et al.*[1] with permission).

The spectrum shown in the **Figure 1.4** is dominated by two intense narrow peaks at the low energy (285-288 eV). The peak at 285 eV (A) is the carbon 1s $\rightarrow \pi^*_{C=C}$ transition of the phenyl functional group and the peak at 287 eV (B) is the carbon 1s $\rightarrow \pi^*_{CN}$ transition of the

acrylonitrile functional group. The transition energy is determined by the combination of initial state effects (the core binding energy) and the final state effects (energy of the unoccupied π* orbital).[1]

Further, NEXAFS spectroscopy has a capability to differentiate different chemical structures in the molecules. To demonstrate these spectral-structural relationships, the carbon 1s spectra of a series of polymers containing unsaturated functional groups, toluene diisocyanate (TDI) urethane, toluene diisocyanate (TDI) urea, methylene diisocyanate (MDI) urethane and methylene diisocyanate (MDI) urea are presented in the **Figure 1.5**.

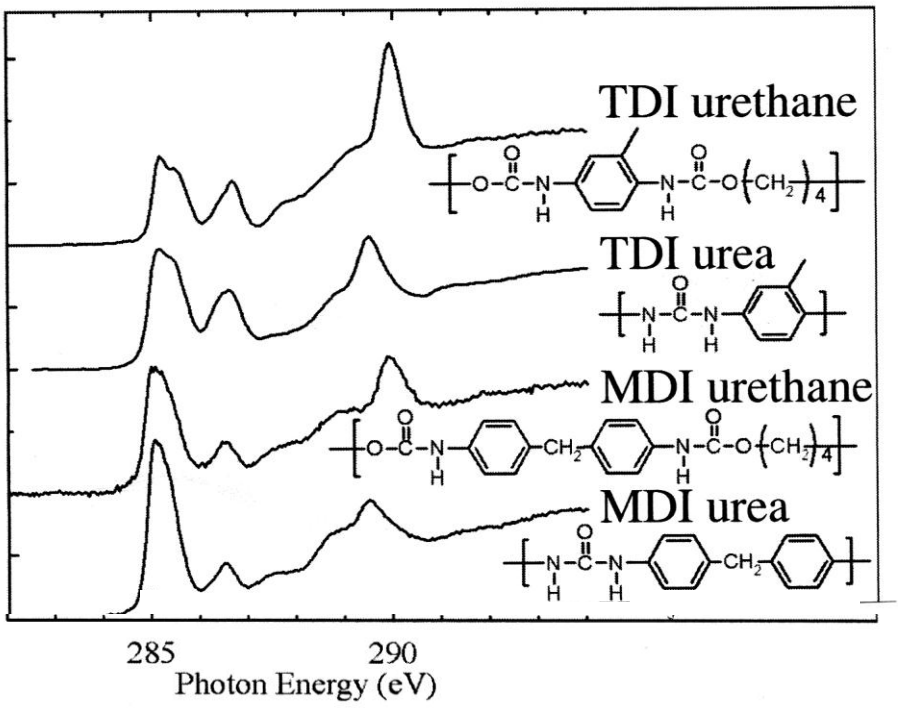

Figure 1.5 Carbon 1s NEXAFS spectra for the series of unsaturated polymers (figure reprinted from Ade *et al.*[1] with permission).

This figure shows that the NEXAFS spectra of these unsaturated polymers are dominated by a low energy carbon 1s (C-H) $\rightarrow \pi^*_{C=C}$ component at ~ 285 eV and a carbon 1s (C-R) $\rightarrow \pi^*_{C=C}$

component at ~ 286.5 eV. Here the specific core level was indicated parenthetically before the arrow, and the upper level is shown from the final subscript in the notation.

In the spectra of TDI polyurea and TDI polyurethane, the carbon 1s (C-H) $\rightarrow \pi^*_{C=C}$ transition appears as a doubly split peak, and carbon 1s (C-R) $\rightarrow \pi^*_{C=C}$ peak where phenyl ring attached to the amide group appears as a single peak at ~ 286.5 eV. Even though both TDI polyurea and TDI polyurethane have an amide group attached to the phenyl carbon, the shape and the energy of the peaks is significantly different due to the different inductive effect of the amide group present in each compound.

In the spectra of MDI polyurea and MDI polyurethane, the C-R (amide) peak (286 eV) is about half as intense as in the TDI polyurea and TDI poly urethane spectra. The intensity of this peak reflects the higher fraction of C-R bonds (amide) per phenyl ring in the TDI polymers.[1] This shows how molecules can be differentiated chemically by carbon 1s NEXAFS spectroscopy. The quality of this application depends on the resolving power of the NEXAFS experiment. In general, an energy resolution better than 100 meV is required to realize all the subtleties in the NEXAFS spectra of polymers.[1]

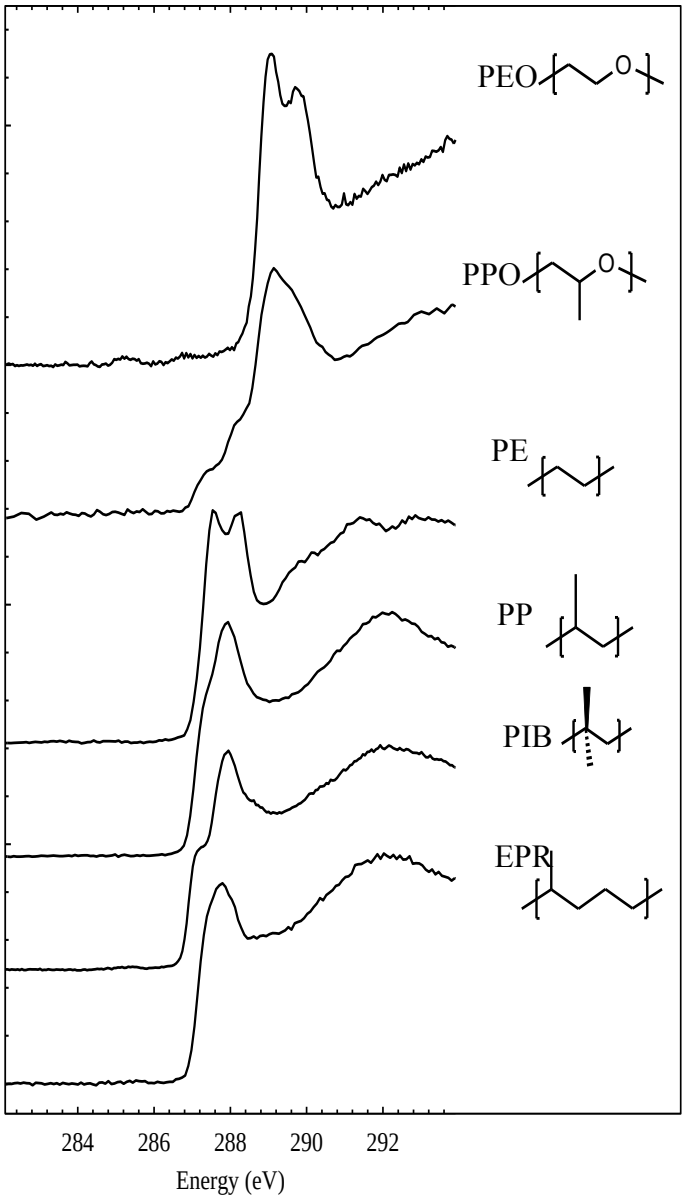

Figure 1.6 Carbon 1s NEXAFS spectra for the series of saturated polymers (figure reprinted from Ade *et al.*[1] with permission).

NEXAFS spectroscopy also can be used to differentiate different saturated polymers such as *n*-alkanes. Core $\rightarrow \sigma^*$ transitions are the dominant transition in the carbon 1s NEXAFS spectra of saturated polymers. The addition of number of methyl groups to the $(CH_2)_x$ back bone is the main difference between the chemical structure of the poly(ethylene) (PE), poly(propylene) (PP) and poly(isobutylene) (PIB) compounds (**Figure 1.6**). The effect of this change can be seen in

the corresponding carbon 1s NEXAFS spectrum of each polymer by looking at the intensity of the low energy shoulder (286-288 eV), as transitions for the CH_3 group appears at this energy. In the NEXAFS spectrum of poly(isobutylene) (PIB), the low energy shoulder is more intense as this polymer has two methyl groups compared to the one in the poly(propylene) (PP) and none in the poly(ethylene) (PE). When the carbon 1s NEXAFS spectra of poly(ethylene) (PE) and poly(propylene) (PP) are compared with that of poly(ethylene oxide) (PEO) and poly(propylene oxide) (PPO), the effect of the oxygen atom in polyethylene oxide (PEO) and polypropylene (PPO) oxide can be identified.[1] PEO and PPO are shifted to higher energy by the increase in the carbon 1s core binding energy induced by the oxygen atom.

1.1.2 Orientation Analysis by NEXAFS Spectroscopy

A relevant aspect of NEXAFS spectroscopy derives from the selection rules and the character of the orbitals involved in the core transitions. Spectral features in the NEXAFS spectra of aligned molecules and polymers exhibit linear dichroism (LD). LD is the anisotropic absorption of linearly polarized electromagnetic radiation (EMR). In NEXAFS spectroscopy, the transitions originate due to dipole transitions from the core level to the unoccupied molecular orbitals. The polarization dependence of the spectra can be used to identify the orientation of the transition dipole moment of the transitions.

The intensity of the electric-dipole allowed transition is proportional to the scalar product of the electric-field vector of the light and the TDM of that particular transition,[4] given by

$$I \propto | E \cdot \mu_{if}|^2 = |E|^2 = |\mu_{if}|^2 \cos^2\theta \qquad (1.4)$$

where E is the polarization of the electric field vector of the X-ray and θ is the angle between E and μ_{if}. This equation shows that the strength of the transition depends on the orientation of the

TDM (μ_{if}) on associated with that transition, relative to the polarization direction E.[4] The maximum probability of the absorption occurs when linearly polarized light (E) is parallel to the TDM (μ_{if}) and minimum probability of the absorption occurs when linearly polarized light (E) is normal to the TDM (μ_{if}).[9-11]

The TDM for a σ^* or π^* transitions is related to the molecular geometry. A π^* TDM is precisely defined for a planar or linear molecule, but for polyatomic molecule, the TDM for a σ^* transition cannot be simply determined. In linear molecules, the electric dipole vector of the final state orbital for the σ^* and π^* transitions are directed parallel and normal to the chemical bond direction. Therefore polarization dependence of the peak intensity can give the direction of the transition moment and that will provide the information of the bond direction and molecular orientation.[1,2,4,5,9-11]

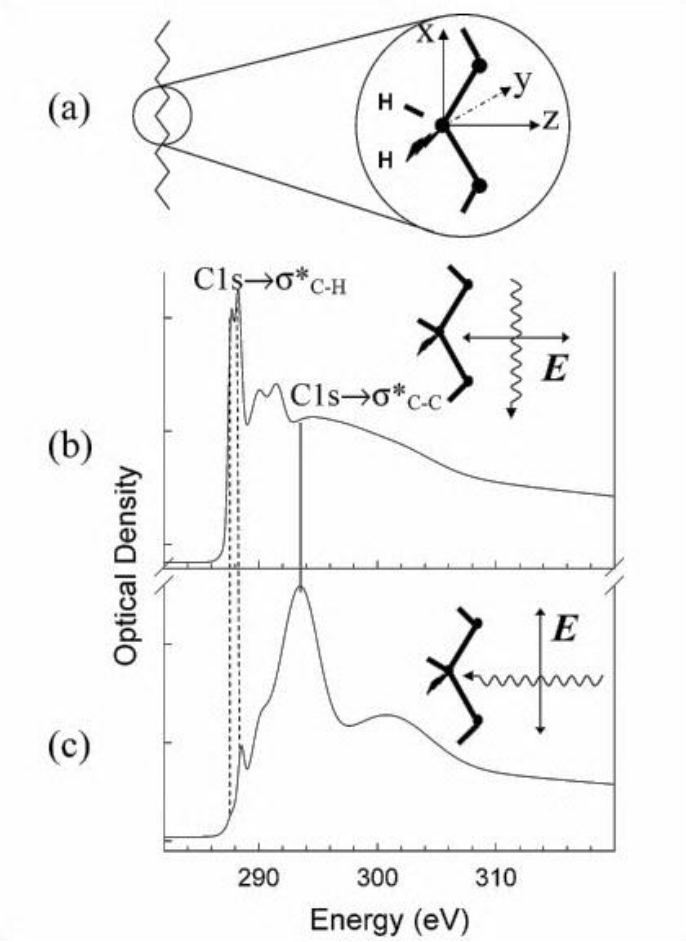

Figure 1.7 a) Schematic of a linear alkane chain and an enlarged view of the geometry of a carbon atom in the chain. The x-axis is the macroscopic chain direction and CH bonds are located in the yz plane. (b) Carbon 1s NEXAFS spectrum, when E ⊥ x-axis (c) Carbon 1s NEXAFS spectrum, when E ∥ x-axis, E is the electric field vector of linearly polarized X-rays (figure reprinted from Fu *et al.*[10] with permission).

Figure 1.7 shows how this works. The direction when the electric field vector E, is perpendicular to the macroscopic chain direction, the maximum intensity occurs for the carbon 1s $\rightarrow \sigma^*_{C\text{-}H}$ transitions (**Figure 1.7b**). When the electric field vector E is parallel to the chain axis, the maximum intensity occurs for the carbon 1s $\rightarrow \sigma^*_{C\text{-}C}$ transitions (**Figure 1.7c**).[9-11] Hence, the molecular orientation can be identified.

1.2 "Matrix Effects" in NEXAFS Spectroscopy

"Matrix effects" are spectroscopic changes induced by intermolecular interactions, providing sensitivity to local structure and order in solids and liquids. The origins of matrix effects are proposed in §1.2.1. Different groups use different experimental approaches to study the origins of the spectroscopic changes induced by intermolecular interactions. As an example, Gillies *et al.*[13] compare the carbon 1s NEXAFS spectrum of neopentane recorded in the gas phase by total ion yield, and in the condensed phase by total electron yield.[13]

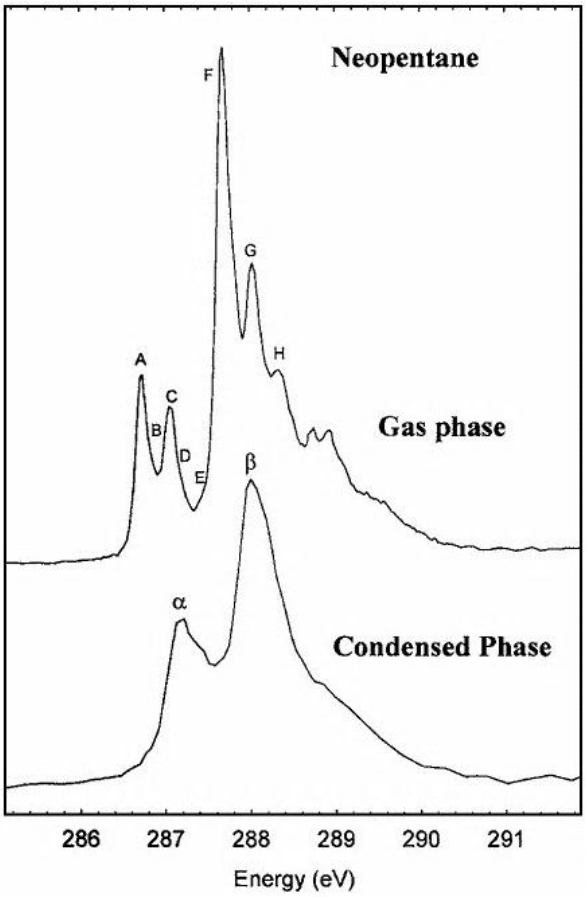

Figure 1.8 Comparison of the carbon 1s NEXAFS spectrum of neopentane, recorded in the gas phase by total ion yield and in the condensed phase by total electron yield (figure reprinted from Gillies *et al.*[13] with permission).

Figure 1.8 shows how the transitions change in shape and energy when the carbon 1s NEXAFS spectrum goes from the gas phase to the condensed phase. The gas phase spectra of the neopentane exhibits many Rydberg peaks in the 286-289 eV region, but in the condensed phase, the spectrum is reduced to two broad peaks. This suggests that the Rydberg character is quenched in the condensed phase. Also, the energy of the peaks is shifted to a higher energy when the carbon 1s NEXAFS spectrum goes to the condensed phase. Hence, "matrix effects" (the effect of intermolecular interactions) change the NEXAFS spectra considerably. Further discussions on the previous experimental approaches for identifying the origins of the matrix effects will be given in §1.2.2. Knowledge of these matrix effects is important to fully understand the spectral behavior of a given species.

1.2.1 Origins of Matrix Effects

Various explanations for the origins of matrix effects are described in the literature. Of these, quenching of Rydberg states,[13-15] dynamic stabilization of core excited states,[16] changes in electronic configuration driven by changes in molecular confirmation,[17] changes due to hydrogen bonding[18,19] and changes in vibronic structure[20] are some of the origins proposed.

1.2.2 Previous Experimental Approaches

Even though they did not use the word "matrix effect", several research groups performed different experiments that can be used to identify matrix effects. Most studies were based on the carbon 1s NEXAFS spectra of gas and condensed alkanes.

The dominant features in the high resolution NEXAFS spectra of simple gas phase alkanes such as methane, ethane, and propane are a progression of carbon 1s $\rightarrow$ Rydberg transitions with rich vibronic structure.[13,21-24] Further, Remmers *et al.*[22] observed the energy separation between the

lowest Rydberg state and highest Rydberg transitions increases from methane to propane. This interpretation was further confirmed by Gillies *et al.*[13] with studies from methane to gaseous neopentane. The gas phase carbon 1s NEXAFS spectrum of small alkanes is predominantly Rydberg in nature.

Unlike the gaseous phase spectrum, several controversial interpretations can be found for the carbon 1s NEXAFS spectra of condensed phase alkanes. Stöhr *et al.*[25] showed that the carbon 1s NEXAFS spectra of condensed alkanes like paraffin thin films and polyethylene are much broader than the gas phase and argued these transitions should be assigned as carbon 1s $\rightarrow \sigma^*_{C\text{-}H}$ transitions.[13,25,26]

Bagus *et al.*[27] proposed that carbon 1s $\rightarrow$ Rydberg transitions are the dominating feature in the NEXAFS spectra of saturated long chain hydrocarbons. They supported their conclusions from *ab initio* calculations of an isolated propane molecule.[27] Further, they predicted that Rydberg features will be shifted to a higher energy in the NEXAFS spectra of condensed saturated hydrocarbons from their *ab initio* calculations on propane trimer and septamer.[13,28,29] Later, they proposed a mixed Rydberg-Valence character for condensed phase octane by performing density functional theory (DFT) calculations.[28]

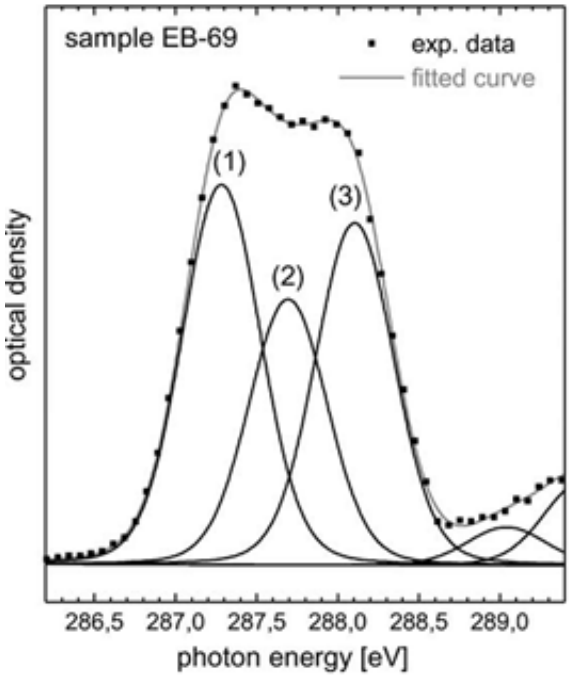

Figure 1.9 Comparison between experimental data and fitted values of the low energy features in the carbon 1s NEXAFS spectrum of polyethylene (figure reprinted from Schöll *et al.*[14] with permission).

Meanwhile, Schöll *et al.*[14] proposed that the low energy features (287-288 eV) in ordered alkanes are not dominated by Rydberg character.[14] In their study, they fitted their experimental peaks observed in the energy range of 287-288 eV (**Figure 1.9**). For a lower sample crystallinity, peaks 1 and 2 in **Figure 1.9** are shifted to lower energy, while peak 3 remained at the same energy. The higher the crystallinity, the lower the spectral intensity of the 287.7 eV peak (peak 2 in **Figure 1.9**), which they assumed had Rydberg character. Due to the lower intensity of peak 2 (**Figure 1.9)** in the high crystalline compound, they claimed that peaks 1 and 3 (287.4 eV and 288.1 eV) have C-H σ* character. This study did not support the conclusions of Bagus *et al.*,[27,28] but their assignments were in agreement with the conclusions of Stöhr *et al.*[25] and Väterlein *et al.*[25,26,30] However, the degree of Rydberg quenching is still under discussion. Schöll *et al.*[14] also concluded that intermolecular interactions play an important role in the spectral variation in the

condensed saturated hydrocarbons and they claimed that complex intermolecular interactions and crystal packing of the molecule can enhance or quench the spectral features as a function of distance.[14]

This interpretation was further supported by the experimental work of Gillies *et al.*[13] They performed carbon 1s NEXAFS spectra of gaseous and condensed neopentane and interpreted the spectral variation using high quality *ab initio* calculations on an isolated molecule and on a cluster designed to model a solid.[13] Gillies *et al.*[13] showed that the degree of Rydberg – valence mixing changes with the condensation of alkanes. Predominantly Rydberg character in the gas phase will change into the valence character in the condensed phase.[13] Further, they concluded the Rydberg character in the solid phase was not entirely quenched, but it converts into a mixed Rydberg-valence state.[13]

However, there is disagreement between the models developed by Bagus *et al.*,[27] Weiss *et al.*,[28] and Gilles *et al.*[13] This is discussed in detail in reference 13 and 31. Intermolecular interactions or "matrix effects" play an important role in the spectral changes observed in carbon 1s NEXAFS spectroscopy of *n*-alkanes.

1.3 Experimental System

The experimental approach and the related literature will be discussed in this section. In this project, the matrix effects in the carbon 1s NEXAFS spectroscopy of *n*-alkanes with different crystal structures will be studied. Different crystal structures of *n*-alkanes were approached in two ways. The first approach was done by varying the *n*-alkane chain length (see §1.3.1 and §1.3.1.1). The other approach was examination of *n*-alkanes through order-disorder transitions at different temperatures (see §1.3.2 and §1.3.2.1).

1.3.1 NEXAFS Spectroscopy of *n*-Alkanes with Different Crystal Structures from Different Chain Lengths

The crystal structure of *n*-alkanes depends on their chain length. *N*-alkanes crystals are orthorhombic for an odd number of carbon atoms, triclinic for even number of carbon atoms (C14-C26) and monoclinic for even when number of carbon atoms C28-C36.[31] For a chain length greater than 36, orthorhombic crystal structures were observed. The crystal structure of the *n*-alkanes used in this project and the related literature studies will be discussed in §1.3.1.1.

1.3.1.1 Crystal Structure of *n*-Alkanes and Previous NEXAFS Measurements

Molecular side packing, end group packing, or both, play an important role in determining a crystal structure and energy of the *n*-alkane crystal lattice.[32] However, there are similarities and differences in the different crystals structure of *n*-alkanes. The regular diamond or parallelogram shape (**Figure 3.1**) was observed from the optical microscopy for all *n*-alkanes crystals with different crystal structures. Further, the long axis of the chains are parallel to each other and have a fully extended all trans configuration.[32]

The differences between the different crystal structures of *n*-alkanes will lead to small but precise differences in the intermolecular interactions between the *n*-alkane chains.

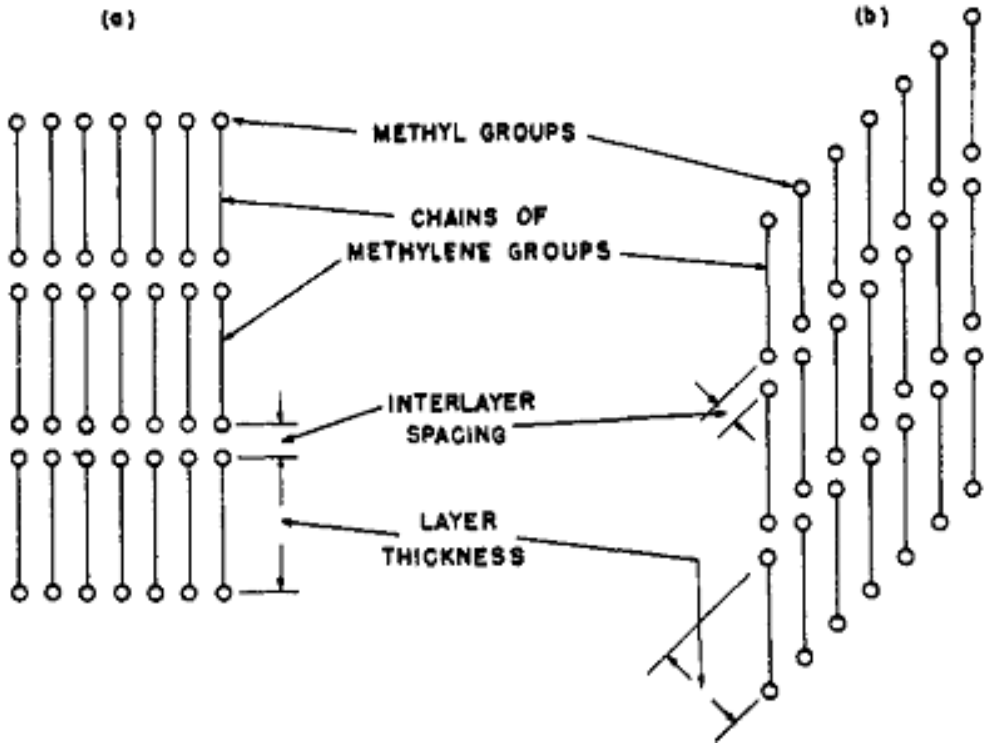

Figure 1.10 Schematic representation of the different arrangement of *n*-alkane molecules different crystal structures. (a) (left) Rectangular layers of orthorhombic structures and (b) (right) oblique layers for triclinic and monoclinic structures (figure reprinted from W.R. Turner, with permission).[32]

Figure 1.10 shows the different arrangements of normal alkane molecules within a layer and the stacking of the layers. According to **Figure 1.10**, orthorhombic crystals have rectangular layers (**Figure 1.10a**) while monoclinic and triclinic crystals have oblique layers (**Figure 1.10b right**). Furthermore, in orthorhombic crystals, the chain axis is perpendicular to the end group plane, while for triclinic and monoclinic crystals, the chain axis is tilted with respect to the end group plane.[32,33] This tilt angle is different for different crystal structures. In the monoclinic crystal structures, the chains make an angle of 61° with the end group plane, while in triclinic crystal structures, they make a 73° angle.[32,33] The displacement of adjacent chains along their axes is about two carbon-carbon units in monoclinic structures, one carbon-carbon unit in the triclinic

structures, and no displacement in the orthorhombic crystal structure of *n*-alkanes.[32] Hence, it is reasonable to expect that each different *n*-alkane crystal structure may have different intermolecular interactions which should lead to changes in this NEXAFS spectroscopy.

Four types of *n*-alkanes (*n*-tricosane ($C_{23}H_{48}$), *n*-tetracosane ($C_{24}H_{50}$), *n*-octacosane ($C_{28}H_{58}$) and *n*-tetracontane ($C_{40}H_{82}$)) cover all the possible different crystal structures in *n*-alkanes were selected. These samples exhibit a single crystal structure at room temperature without polymorphism. Further, high purity in those samples will minimize the effect that comes from the common impurity in *n*-alkanes of slightly different chain lengths. If an impurity *n*-alkane molecule is deposited on the growth front of a crystal, the impurity *n*-alkane will misfit to the chain ends in the host lattice and a different structure conversion may result.[32,33] As an example, a very small quantity of impurities can convert a triclinic structure into a monoclinic structure, and more than 10% of mole fraction can convert the system into orthorhombic crystal structure as well.[32,33]

Previous literature identified that *n*-tricosane ($C_{23}H_{48}$) has an orthorhombic crystal structure as its stable structure at room temperature.[31,34-38] Similarly *n*-tetracosane ($C_{24}H_{50}$) is triclinic,[31,36,39] *n*-octacosane ($C_{28}H_{58}$) is monoclinic[31,36,38] and *n*-tetracontane ($C_{40}H_{82}$) has an orthorhombic crystal structure at room temperature.[31,40]

Previous NEXAFS measurements

Previous studies have examined different aspects of the NEXAFS spectra of solid *n*-alkanes, such as orientational effects induced by *n*-alkane film deposition, chain length effects and the van der Waals interactions between alkane molecules.

Fu *et al.*[11] worked to identify the changes which result in the carbon 1s NEXAFS spectroscopy of condensed phase *n*-alkanes due to their orientation. They found an effect of chain length and substrate temperature on the morphology and molecular orientation of the solid *n*-alkane thin films.[10,11] Fu *et al.*[11] concluded that longer chain *n*-alkanes like *n*-hexacontane ($C_{60}H_{122}$) are oriented laterally due to the stronger interaction between molecules and the NaCl (001) substrate, while shorter chain *n*-alkanes like *n*-hexatriacontane ($C_{36}H_{74}$) are only partially oriented due to their lower interaction strengths.[9-11]

Meanwhile, Gillies *et al.*[13] measured the carbon 1s NEXAFS spectra of condensed phase neopentane.[13] They found two broad peaks in the low energy C-H region (287-288 eV) of the spectra (**Figure 1.8**)[13] and assigned these as carbon 1s $\rightarrow \sigma^*_{C\text{-}H}$ transitions. This was supported by Scholl *et al.*[14] on ethylene-1-alkene copolymers with various concentrations of side chains,[14] who reported that the appearance of the split peak in the carbon 1s $\rightarrow \sigma^*_{C\text{-}H}$ resonance (287-288 eV) that was directly correlated with the polymer crystallinity.[14] Hence, for low branching ratio and short branch length of the copolymers, double peaks were visible at 287.4 and 288.1 eV, while for high branching ratio and long copolymers branch length, only a single broad peak was visible.[14] Scholl *et al.*[14] observed that the double peak structure disappears as the crystallinity decreased. On the basis of *ab initio* calculations, they concluded these two peaks have a resolvable $\sigma^*_{C\text{-}H}$ / Rydberg resonant character (**Figure 1.9)**.[14,15,30,41]

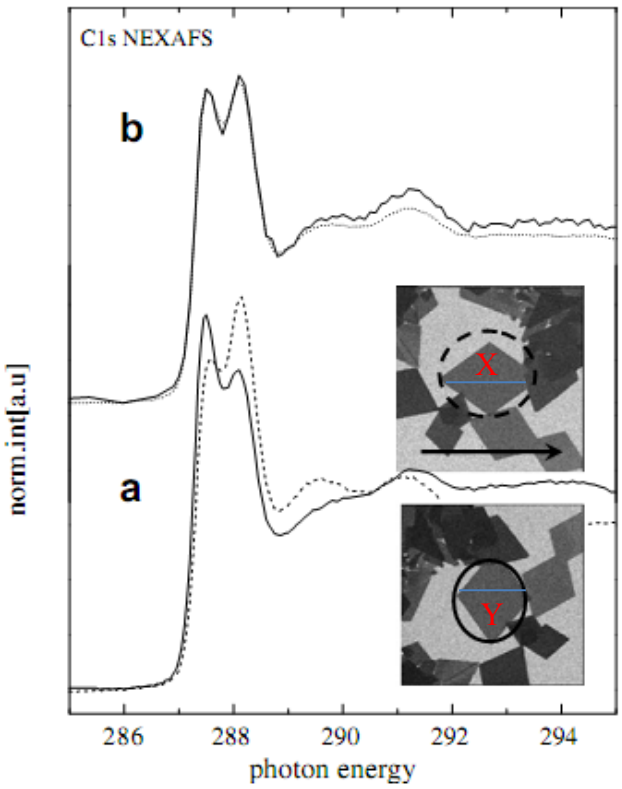

Figure 1.11 (a) Carbon 1s NEXAFS spectra of the *n*-tetracontane ($C_{40}H_{82}$) crystal in the center of the images recorded by STXM at 288.0 eV. Solid line spectrum recorded from crystal with Y axis aligned with horizontally polarized photon beam, dashed line from the same crystal with X axis aligned horizontally after rotation of the sample by 90°. (b) Carbon 1s NEXAFS spectrum of *n*-tetracontane ($C_{40}H_{82}$) crystal recorded with circular polarized light (solid line), compared with the sum spectrum (dotted line) derived from (a) (figure reprinted from Zou *et al.*[41] with permission).

Recently, Zou *et al.*[41] studied effect of intermolecular interactions between *n*-alkanes molecules by carbon 1s NEXAFS spectroscopy. They reported a relationship between the intensity of these two low energy peaks and the X and Y axis orientation of single crystals of *n*-tetracontane ($C_{40}H_{82}$) and *n*-nonadecane ($C_{19}H_{40}$) (**Figure 1.11**).[41] When the polarization is directed along the X direction, the relative intensity of the first C-H peak was lower than the second C-H peak, and when the polarization is directed along the Y direction, the relative intensity of the first C-H peak was higher than the second C-H peak. Therefore just a fractional change in the weak Van der Waals interactions will modify significantly the intensity, spectral shape, peak position, and dichroic signature in the NEXAFS spectrum of *n*-alkane.[15,41]

Although different aspects of solid state effects have been previously observed, there is not a complete understanding of the complicated behavior of the NEXAFS spectra. Therefore, we will use NEXAFS spectroscopy to study exceptionally well defined crystal structure materials in the form of single alkane crystals with well-defined orientations. Single *n*-alkane crystals were prepared using a solution casting method, and a systematic experimental approach is used to identify the changes observed in the NEXAFS spectroscopy of *n*-alkane crystals which vary by chain length and through the order-disorder transitions.

1.3.2 NEXAFS Spectroscopy of *n*-Alkanes through Order-Disorder Transitions

In order to identify the changes observed in NEXAFS spectroscopy of *n*-alkanes with respect to the order-disorder transitions, it is important to know what possible order-disorder transitions exist, and the corresponding temperatures of these transitions. This will be discussed in §1.3.2.1. Early temperature dependent studies on the NEXAFS spectroscopy of *n*-alkanes will be discussed in §1.3.2.2.

1.3.2.1 Order-Disorder Transitions of *n*-Alkanes

Two polymorphous solid phases can be found in *n*-alkanes. At low temperatures, a crystalline or ordered phase is observed and at high temperature, a disordered or rotator phase is observed. These major phases can be differentiated by the spectral and structural changes observed in the solid structure below the melting point.[42] In addition, some odd-numbered *n*-alkanes undergo other order-order transitions as well.[42] **Figure 1.12** presents all the observed order-order, order-disorder and disorder-disorder transitions in *n*-alkanes with respect to the different chain length.

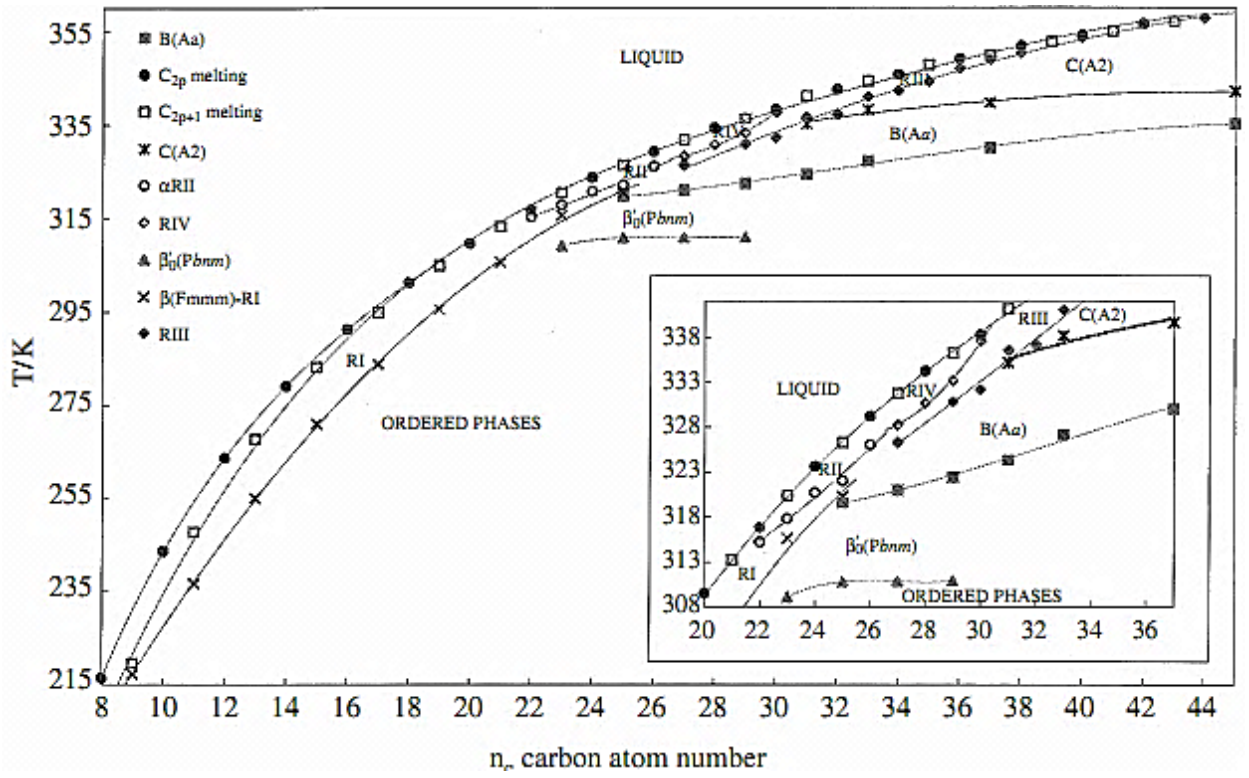

Figure 1.12 Sequence of the phases with temperature (K) and the evolution of (solid + solid) and (solid+ liquid) transition temperatures of pure *n*-alkanes ($8 \leq n \leq 45$) as a function of the carbon atom number n (figure reprinted from Dirand *et al.*[42] with permission).

In the literature, different techniques were used to identifying the *n*-alkanes phase transitions. Differential Scanning Calorimetry (DSC) is widely used. This project is focused on four *n*-alkanes which represent three possible crystal structures of *n*-alkane systems. Tricosane ($C_{23}H_{48}$ - orthrombic), tetracosane ($C_{24}H_{50}$ - triclinic), octacosane ($C_{28}H_{58}$ - monoclinic) and tetracontane ($C_{40}H_{82}$ - orthrombic). **Table 1.1** summarizes the phase transitions temperatures from the literature for these *n*-alkanes.

Table 1.1 Reported literature DSC measurements of the *n*-alkanes.

Type of *n*-alkane	References	Crystal – Rotator transition/ °C	Rotator– Rotator transition/ °C	Melting point/ °C
n-tricosane ($C_{23}H_{48}$)	Sirota *et al.*[36]	40.17	47.75	47.24
	Chevallier *et al.*[37]	40.70	45.50	47.76
	Dirand *et al.*[42]	42.45	-	47.55
	Kraack *et al.*[38]	40.60		47.20
n-tetracosane ($C_{24}H_{50}$)	Sirota *et al.*[36]	47.90	46.85	50.43
	Dirand *et al.*[42]	47.55	-	50.45
	Kraack *et al.*[38]	47.80		50.40
n-octacosane ($C_{28}H_{58}$)	Dirand *et al.*[42]	57.35	-	61.05
	Sirota *et al.*[36]	57.97	57.35	60.97
	Kraack *et al.*[38]	57.70		60.90
n-tetracontane ($C_{40}H_{82}$)	Dirand *et al.*[42]	80.35	-	80.85
	Wang *et al.*[40]	74.55		80.84

With the exception of *n*-tetracontane ($C_{40}H_{82}$), the phase transition temperature for the order-disorder transitions reported by different groups are similar to each other. The slight variation may arise due to the quality of the DSC instrument or sample purity. Depending on the quality of the experiment, some groups were unable to identify the temperature for the rotator-rotator (disorder-disorder) transition.

In *n*-tetracontane ($C_{40}H_{82}$), Dirand *et al.*[42] reported the crystal-rotator transition at 80.35 °C. Meanwhile Wang *et al.*[40] mentioned that phase transition was observed in the temperature range

of 73.00 °C - 75.00 °C for *n*-tetracontane ($C_{40}H_{82}$) but this phase transition was not a crystal-rotator transition.

X-ray diffraction was used to identify the possible structure in the crystal and rotator phases. In *n*-tricosane ($C_{23}H_{48}$), two types of rotator phases, low temperature orthorhombic rotator and high temperature hexagonal rotator were identified by Doucet *et al.*[35] Nozaki *et al.*[43] identified crystal ordered phases V, IV and III for the same *n*-alkane at relatively high temperatures from X-ray diffraction measurements. Chazhengina *et al.*[34] found another transition in the temperature range of 36.8 - 37.5 °C below the low temperature rotator transition for the same *n*-alkane.

Similarly for *n*-tetracosane ($C_{24}H_{50}$), Denicolo *et al.*[44] mentioned that only a low temperature orthorhombic rotator phase was observed, while Kotelnikova *et al.*[39] reported a triclinic-to-orthorhombic phase transition in the interval 42.2 - 43.3 °C and an orthorhombic-to-hexagonal phase transition at 43.8 °C from their X-ray diffraction studies.

The order-disorder transition values reported from X-ray diffraction techniques were slightly different than the temperature values reported from the DSC for the phase transitions of *n*-alkanes. However this literature data was adequate to select temperatures for the NEXAFS spectroscopy measurements of *n*-alkane molecules used in this project.

1.3.2.2 Previous Temperature Dependent NEXAFS Spectroscopy of *n*-Alkanes

Schöll *et al.*,[14] Fu *et al.*,[11] and Yamamoto *et al.*[45] examined some aspects of the temperature dependent NEXAFS spectroscopy of *n*-alkanes.

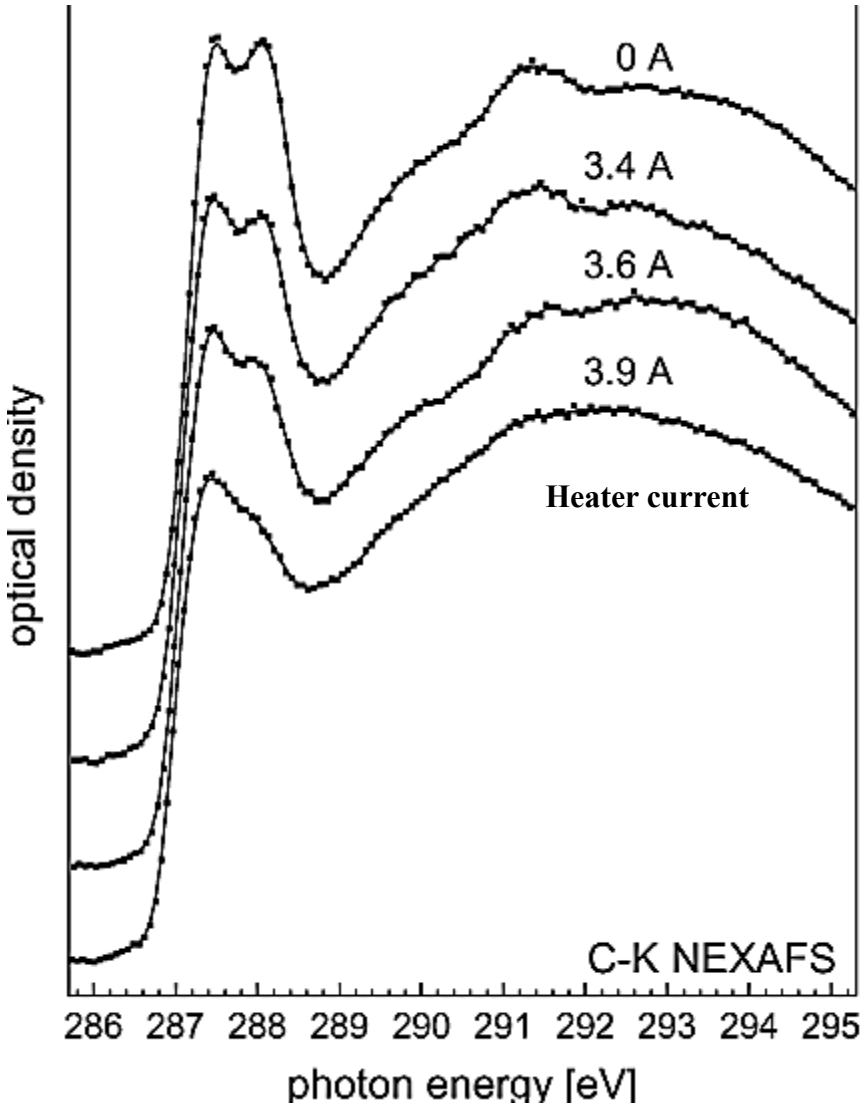

Figure 1.13 Variation of the carbon 1s NEXAFS spectra of low branching ratio and short branch length ethylene-1-butene with heater current (proportional to temperature) (figure reprinted from Schöll *et al.*[14] with permission).

Schöll *et al.*[14] examined the variation in the carbon 1s NEXAFS spectra with crystallinity in co-polymers with temperature. They heated low branching ratio and short branch length ethylene-1-butene polymers to their melting point and observed the variation in the carbon 1s NEXAFS spectra. They measured the temperature indirectly from the heater current as shown in **Figure 1.13**. The sample was destroyed at a heater current of 3.9 Amp, which they concluded that this current corresponded to the melting point. The double peak structure found in the energy region

of 287-288 eV vanished with the increase in temperature and one broad peak appeared at high temperature (3.9 Amp). They concluded that this change occurred as the crystallinity decreased with increased temperature.[14] In a separate experiment, they verified the reversibility of this crystalline-amorphous phase transition by heating the same sample until the double peak structure disappeared, and subsequently cooled the sample till the original spectrum returned.[14]

Yamamoto *et al.*[45] investigated the change of the surface structure of pentacontane ($C_{50}H_{102}$) over a wide temperature range. They observed a ordered structure at the surface of the liquid phase of the alkane, even above the bulk melting point.[45]

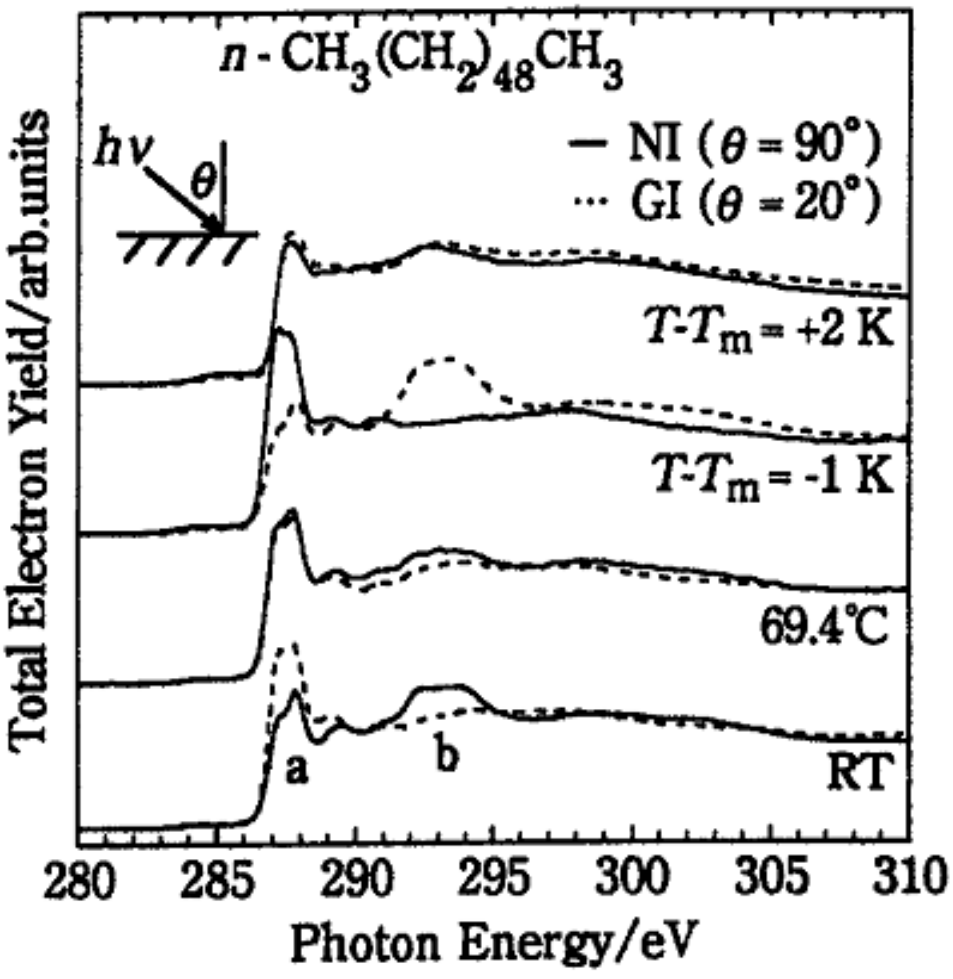

Figure1.14 Temperature dependence of carbon 1s NEXAFS spectra of *n*-$CH_3(CH_2)_{48}CH_3$ (figure reprinted from Yamamoto *et al.*[45] with permission).

Yamamoto *et al.*[45] found that at room temperature, the long molecular axis of pentacontane ($C_{50}H_{102}$) was almost parallel to the substrate, and that during the heating process, these chains oriented perpendicular to the substrate at a temperature just below its melting point.[45] Furthermore, as shown in **Figure 1.14,** they claimed that the *n*-alkane did not reorient during the cooling process, and that process was irreversible.

These temperature driven NEXAFS spectroscopy measurements, while not directly related with our work, are still useful to get an idea about how chains behave at higher temperatures.[45] In our work we will deposit *n*-alkanes crystals on the substrate at room temperature and obtain NEXAFS measurements while heating the sample up to its melting point.

1.4 Research Objectives

In this project, the main goal is to identify the role of matrix effects in carbon 1s NEXAFS spectra, caused by different crystalline *n*-alkane structures. Two experimental approaches were proposed. One identified changes in the carbon 1s NEXAFS spectra of *n*-alkane chains as a function of crystal structure at room temperature, and other identified changes in the carbon 1s NEXAFS spectra of *n*-alkane chains through the order-disorder phase transitions. These changes are related to the expected structural changes.

2. Experimental Methods

2.1 *n*-Alkane Candidates

N-alkanes are a basic type of organic molecule. These molecules play an important role in the properties of the complex molecules such as liquid crystals, proteins and lipids. The linear *n*-alkanes used in this study are *n*-tricosane (*n*-$C_{23}H_{48}$) (Sigma-Aldrich, 99%), *n*-tetracosane (*n*-$C_{24}H_{50}$) (Sigma-Aldrich, 99%), *n*-octacosane ($C_{28}H_{58}$) (Alfa Aesar, 99%) and *n*-tetracontane ($C_{40}H_{82}$) (Alfa Aesar, 97%). These *n*-alkanes were used without purification. These *n*-alkanes molecules were selected in this project due to the reasons mentioned in §1.3.1.1.

2.1.1 Sample Purity

Melting points were determined by Differential Scanning Calorimetry (DSC). The purity of the samples was determined by examining how close the melting point values are with respect to the literature DSC values. The DSC spectrum for the *n*-tricosane ($C_{23}H_{48}$) is shown below.

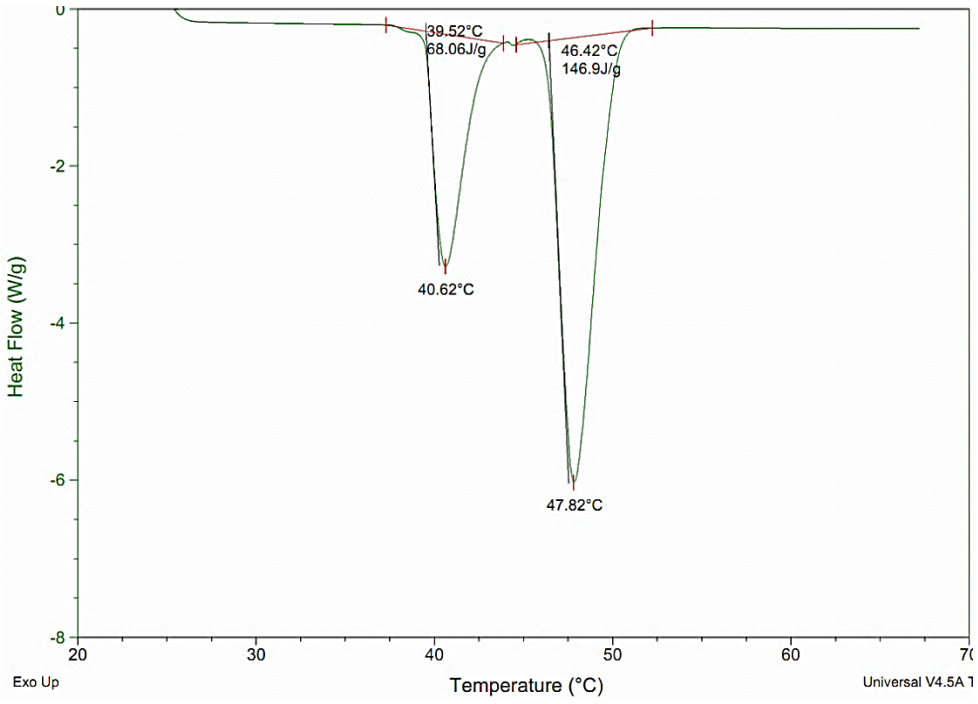

Figure 2.1 DSC spectrum of the *n*-tricosane ($C_{23}H_{48}$).

The corresponding melting point and the order-disorder transitions observed for each *n*-alkane by DSC were presented in **Table 2.1**

Table 2.1 Comparison of measured *n*-alkane melting points with literature values.

Type of *n*-alkane	References	Crystal–Rotator transition/°C	Rotator–Rotator transition /°C	Melting point/°C
n-tricosane (n-$C_{23}H_{48}$)	Sirota *et al.*[36]	40.17	44.75	47.24
	Our work	40.62	-	47.82
n-tetracosane (n-$C_{24}H_{50}$)	Sirota *et al.*[36]	47.90	46.85	50.43
	Our work	48.25	-	50.98
n-octacosane (n-$C_{28}H_{58}$)	Sirota *et al.*[36]	57.97	57.35	60.97
	Our work	58.54	-	61.73
n-tetracontane (n-$C_{40}H_{82}$)	Wang *et al.*[40]	74.55		80.84
	Our work	74.92		80.63

According to **Table 2.1**, the observed temperatures for the crystal – rotator transitions in a given *n*-alkane were in a good agreement (± 0.7 °C) with the reported literature values.[36,38] This is used to confirm that the sample was adequately pure.

2.2 Solution Casting Method

Single *n*-alkane crystals were prepared using a solution casting method. The sample was dissolved in a suitable solvent, and a drop of this solution was placed on a suitable substrate, and the solvent was allowed to evaporate. The temperature, solvent, solvent/sample ratio, and the substrate were varied and for optimized different *n*-alkane samples. In this project, toluene and

isopropyl alcohol were used for the *n*-tetracontane ($C_{40}H_{82}$) and *n*-octacosane ($C_{28}H_{58}$) and methanol was used for the *n*-tetracosane ($C_{24}H_{50}$) and *n*-tricosane ($C_{23}H_{48}$) *n*-alkanes.

2.3 *In situ* Heating Cell Measurements for *n*-Alkane NEXAFS Spectra

2.3.1 Initial Design of the Heating Cell

In the second part of this research project, the variation of the carbon 1s NEXAFS spectra through the pre melting phases of *n*-alkane samples were identified by heating the samples. A heating cell purchased from Adam Leontowich (McMaster University). The accuracy and the stability of the temperature are the most important for these experiments, as the temperature must remain stable during the NEXAFS scan. The original design in the heating cell is shown in **Figure 2.2**.

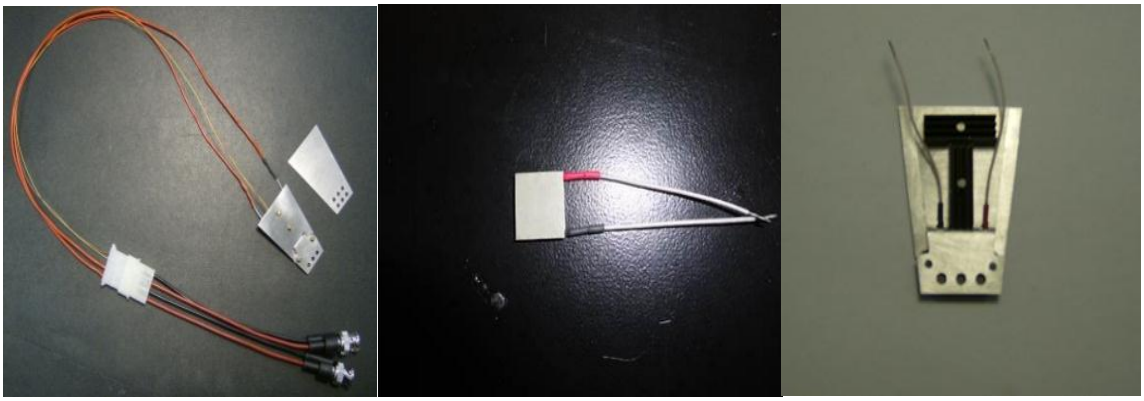

Figure 2.2 (left) Initial design of the heating cell with (middle) the K-type Peltier heater and (right) black heat sinks.

The initial heating device consists of a K-type thermocouple, a Peltier heater and heat sinks. BNC cables connect the thermocouple plug to a standard K-type electrical thermometer (Fluke 52ii) and the Peltier heater (Model: TE technology-65-0.6-0.8) to a power supply (Kepko bipolar power supply).

In this design, (**Figure 2.2**), the Peltier heater acts as a heating device, and the temperature can be controlled by varying the power supply. Even though rating of the Peltier heater was up to 80 °C, this system can reach up 270 °C. The sample mount and heater are thermally insulated from the microscope mount, and heat sinks help dissipate heat on the sample holder (or sample mount).

The accuracy of the device was determined by comparing the observed melting point of the given *n*-alkane to the reported literature melting point value. The stability of the temperature was determined by the ability of the device to maintain the temperature at a particular value. In order to reach the project expectations, the observed melting point of the given *n*-alkane should be similar to its corresponding literature melting point, with a good temperature stability.

When this initial heating cell was operated in air, each *n*-alkane melted more than ± 2 °C away from the corresponding literature melting point value.[31,34,36-38,40] There was also difficulty in maintaining a fixed temperature. These difficulties became worse when the heating cell was mounted inside the STXM chamber, where the temperature was observed to fluctuate widely. This was found to be due to a poor connection in the thermocouple wire and not an actual temperature instability.

2.3.2 Modification to the Heating Cell

The modification of the BNC connections of the original design is shown in **Figure 2.3**.

Figure 2.3 (left) Heating cell before and (right) after modifying the thermocouple connections.

In this setup, wiring was improved to eliminate the problems due to poor connections (**Figure 2.3** right).

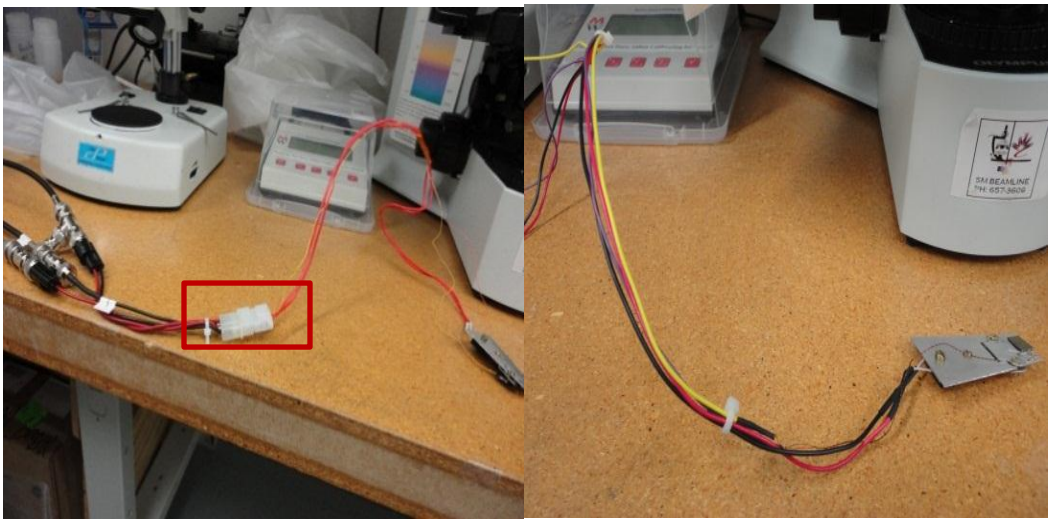

Figure 2.4 (left) Heating cell before and (right) after modifying the thermocouple connections.

The setup shown in **Figure 2.3** was still unable to give reproducible temperature accuracy and setup was modified further as shown in **Figure 2.4**. This setup gave reproducibly accurate

temperature in air. But when the same temperature measurements were performed inside the STXM chamber under vacuum, this cell could not give correct temperature readings through the phase transitions and melting point. The cell was always fluctuated 4-5 °C from the expected literature values. Also, the time needed to reach to the set temperature in the heating device increased with desired temperature. As an example, it took 10 minutes to reach 40 °C and 20 minutes to reach 64 °C. The heating cell was further modified by changing the heater power controller and the heat measuring sensor.

2.3.3 Improvement to Temperature Sensor and Controller

As shown in **Figure 2.5**, the heating cell was further modified by replacing the temperature measuring sensor thermocouple with a thermistor. The power supply was changed to a Proportional-Integral-Derivative (PID) device for temperature regulation.

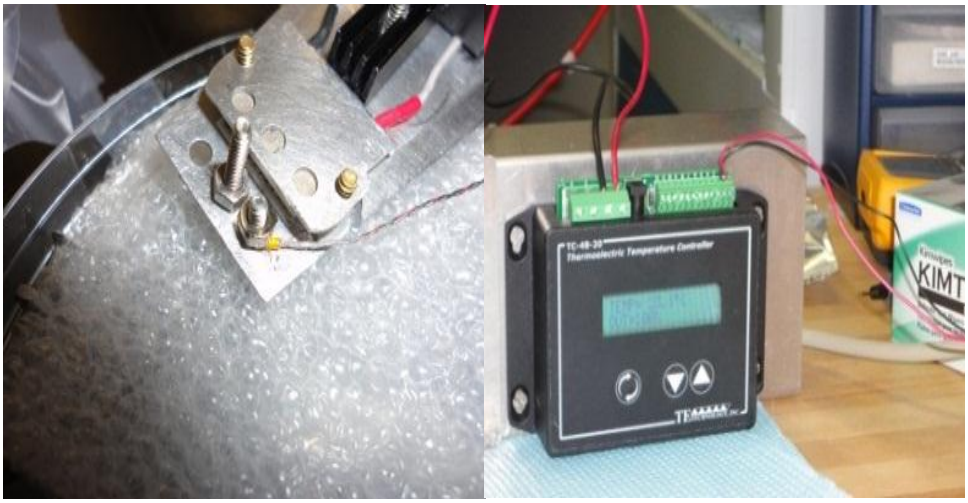

Figure 2.5 Third modification of the heating cell where (left) thermistor was attached to the heating cell and (right) with a temperature controller.

The initial controller (Model: TE technology-65-0.6-0.8) could not be properly calibrated, so this was replaced by an Omega (CN8500 series 1/16 DIN temperature and process controller) controller with the help of Garth Parry of the Chemistry Electronic Shop (**Figure 2.6)**.

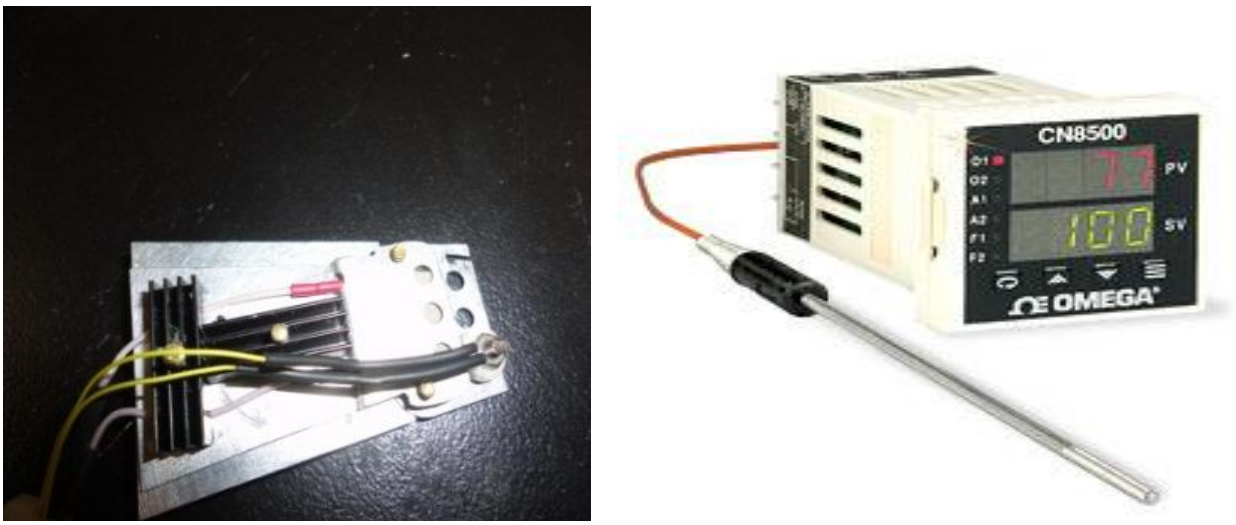

Figure 2.6 Final modification of the heating cell with (left) the RTD element attached to the heating cell and (right) the temperature controller.

In addition, the thermistor was replaced by the Resistance Temperature Device (RTD) (W581 platinum thin film) in order to obtain more accurate temperature reading. This device is more accurate and has less drift.

This device gave accurate and reproducible temperature measurements in air. However, but the temperature reading still fluctuated rapidly when disturbed by air flow, presumably due to uneven convection behavior. This was not an issue when the cell is mounted inside the STXM, under vacuum (< 200mTorr). The temperature reading was accurate and stable in vacuum for up to 10 minutes, with a temperature variation of ± 0.2 °C. The heater reaches to a set temperature within 2-3 minutes, and remained stable. This setup gave an accurate and stabled reproducible temperature reading.

2.4 Characterization of *n*-Alkane Crystals

The morphology, orientation and shape of the different *n*-alkane crystals prepared by solution casting were initially characterized by polarized Optical Microscopy (OM). Further investigation

of the *n*-alkane crystals was done by Scanning Transmission X-ray Microscopy (STXM) at Canadian Light Source, Saskatoon, SK, Canada.

2.4.1 Optical Microscopy

Optical microscopy is a critical tool in material science and chemistry. In order to get the optimal results in a given application, the microscope should be precisely aligned and equipped with high-quality optics (objectives, eyepieces, and condensers), and make use of the appropriate light sources, filters, and contrast enhancement devices.

The objective lens and eye piece are the two components in the microscope that are critical for forming an image. First, the objective lens creates an image of the object in the intermediate image plane. This image in turn can be mapped by with another lens, the eye-piece, which provides further magnification of the object.[46]

In order to get a high quality image, magnification and resolution of the instrument are very important. The resolution of optical microscopy is limited by light diffraction. Equation 2.1 shows the smallest distance (d_{min}) can be resolved between point sources.

$$d_{min} = 1.22\times(\lambda/2NA) \qquad (2.1)$$

Where NA = n×sinα was called numerical aperture of the objective lens, n was the index of the refraction in the object space, λ is the wavelength of the light and α is the half maximal angle under which the objective lens collects light from the object. Usually, a large numerical aperture of the objective will improve the spatial resolution and brightness of the image.[46]

Different contrast enhancements can be used to obtain more information or contrast from the images. Bright field, dark field, phase, fluorescence and polarization are some of the contrast

modes available in optical microscopy. In this study, optical microscopy images were taken in epi-illumination bright field polarized optical microscopy mode.

Epi-Illumination Bright Field Polarized Optical Microscopy

The schematic diagram of a polarized optical microscope is shown in **Figure 2.7**.

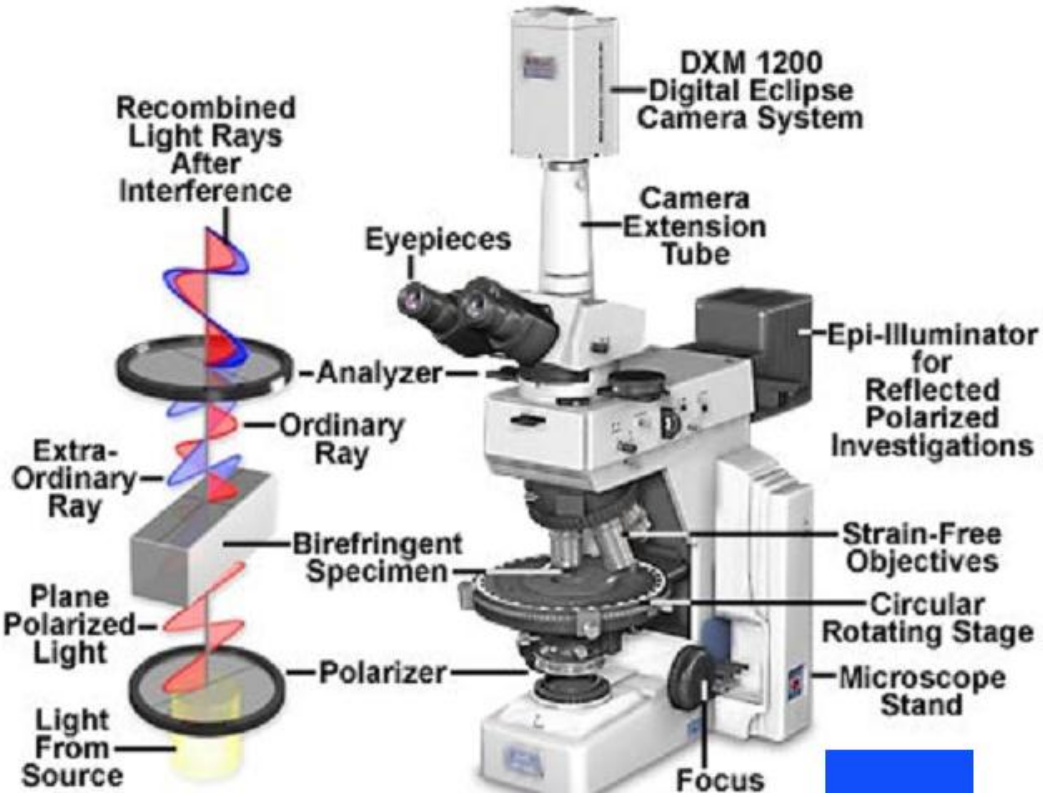

Figure 2.7 Schematic diagram of the polarized optical microscope (figure reprinted from reference 47, with permission).[47]

According to **Figure 2.7**, light from an incandescent source is passed through a polarizer which makes electric field vector of light restricted to a single direction by filtration. The beam was passed through the condenser lens and specimen (object). When a specimen has adjacent regions that differ in refractive index, they refract the light differently. When the light is recombined by a second prism in the objective lens, differences in brightness correspond to differences in the

sample birefringence.[46] Color contrast occurs because when the refractive index depends on the wavelength and varies from point to point in the object.[46]

2.4.2 Scanning Transmission X-ray Microscopy (STXM)

X-ray Radiation

In 1895, W.C Röntgen observed the X-ray for the first time and he was awarded the physics Nobel prize in 1901 for his observation. In order to get the NEXAFS spectroscopy from the STXM, a tunable, collimated and coherent source of radiation with high photon flux and ideal polarization conditions is required. In this project, an elliptically polarized undulator was used to produce X-rays for the experiments.

Polarization of the X-ray Radiation

Electromagnetic radiation is composed by electric (E) and magnetic field (H) components. These oscillate at right angles to one another and perpendicular to the direction of the propagation. The polarization is described by the electric field vector.

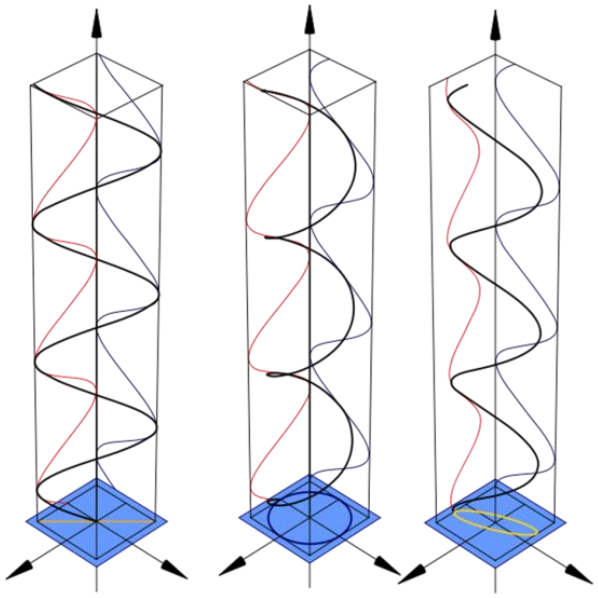

Figure 2.8 Schematic diagram for (left) linearly polarized X-ray radiation, (middle) circularly polarized X-ray radiation and (right) elliptically polarized X-ray radiation (figure reprinted from reference 48, under creative commons license).[48]

Linear, circular and elliptical are the three main types of polarization of radiation. **Figure 2.8** shows the electric field vector (black) with the time (vertical axis) at a particular point along with its X and Y components (Red and blue line). The paths of each types of polarization are shown in the bottom of the vector in the plane (yellow in left and right image and purple in middle image).

For linear polarized X-ray radiation, the electric field vector oscillates in a single plane (**Figure 2.8** left). In circular polarized radiation, the electric field vector precesses in a circular path (**Figure 2.8** middle), and can have a left and right handed circular polarization. When looking at the beam coming towards you, a clockwise rotation will generate the right circularly polarized radiation (RCP) and an anticlockwise rotation will generate left circularly polarized (LCP) radiation.

In elliptically polarized radiation, the electric field vector oscillates in an elliptical pathway (**Figure 2.8** right). This is an intermediate between linear and circular polarization.

Synchrotron Radiation

A synchrotron facility consists of storage ring and an electron beam source. Initially, electrons produced by an electron gun (~10′s of MeV) are accelerated by straight sections (linear accelerator) up to a several hundreds of MeV, and this is further increased by a booster to a several GeV, and then injected into a storage ring. The electromagnetic radiation is emitted from the storage ring with the aid of bending magnet (BM) or insertion devices (ID) such as wigglers and undulators. Schematic representation of bending magnet, wiggler and undulator is presented in **Figure 2.9**.[49]

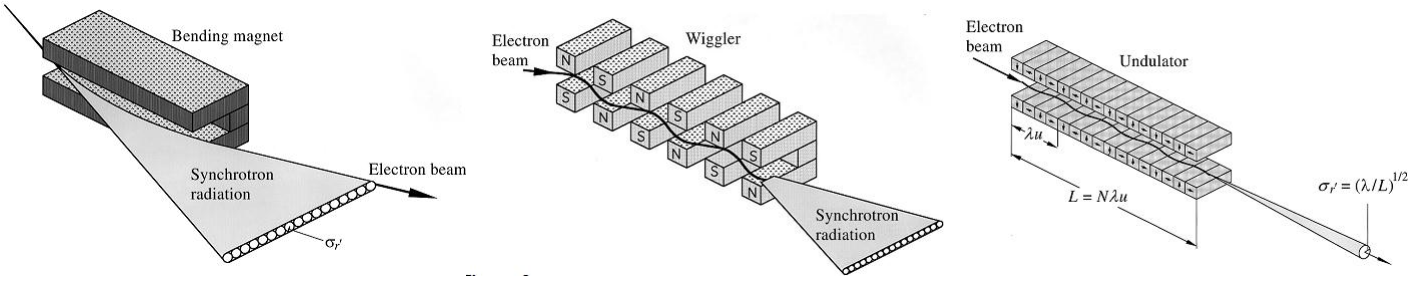

Figure 2.9 Schematic representation of a bending magnet, a wiggler and a undulator (figure reprinted from H. Kitamura, with permission).[49]

Figure 2.9 shows that a BM produces radiation in a wide cone. The energy distribution can be shifted to higher energy by increasing the bending magnetic field or introducing a higher energy ring. But this has major practical issues and cost issues.[49]

Wigglers and undulators are two types of IDs. **Figure 2.9** shows that wigglers are composed of many magnets with opposite polarities. The intensity of the radiation produced from wigglers

can be increased by increasing the number of magnets. In addition, the large oscillation amplitude formed by the large magnetic field in wigglers creates larger cone of radiation (**Figure 2.9**).[49,50]

In contrast, smaller oscillation amplitudes formed by the smaller magnetic field in undulators creates a narrow cone of radiation (**Figure 2.9**). The energy of this radiation is changed by altering the gap between two rows of magnets. Both wigglers and undulators produce linearly polarized radiation in the plane of the row of magnets.

An Elliptically Polarized Undulator (EPU) uses four quadrants of periodic magnets to generate different polarity of synchrotron radiation. In an EPU, a row of two quadrants is placed above the electron path way and two are below the electron path way as shown in **Figure 2.10**.

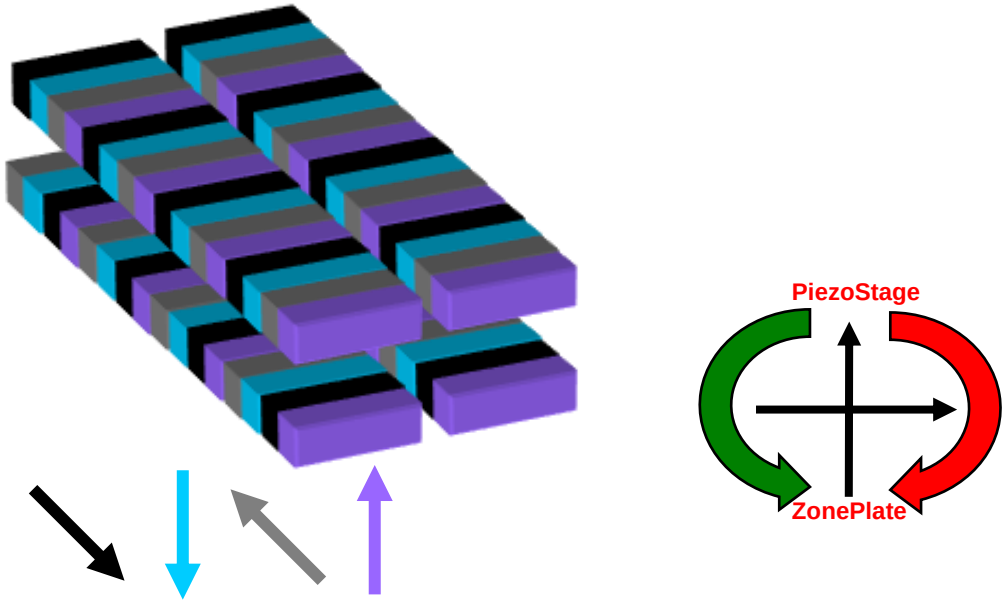

Figure 2.10 The schematic diagram of (left) an elliptically polarized undulator and (right) the possible types of polarization from an EPU.

In each row, one quadrant is fixed and the other can move longitudinally along the electron path way. The translation of the four quadrants will change the phase between vertical and horizontal components of the magnetic field (**Figure 2.10** left). Hence, the EPU has the ability to deliver fully circular polarized light (LCP and RCP) and fully elliptically and linearly polarized light (**Figure 2.10** right). The latter is achieved by rotating the electric vector of the light in the range of +90°- 90°.[51]

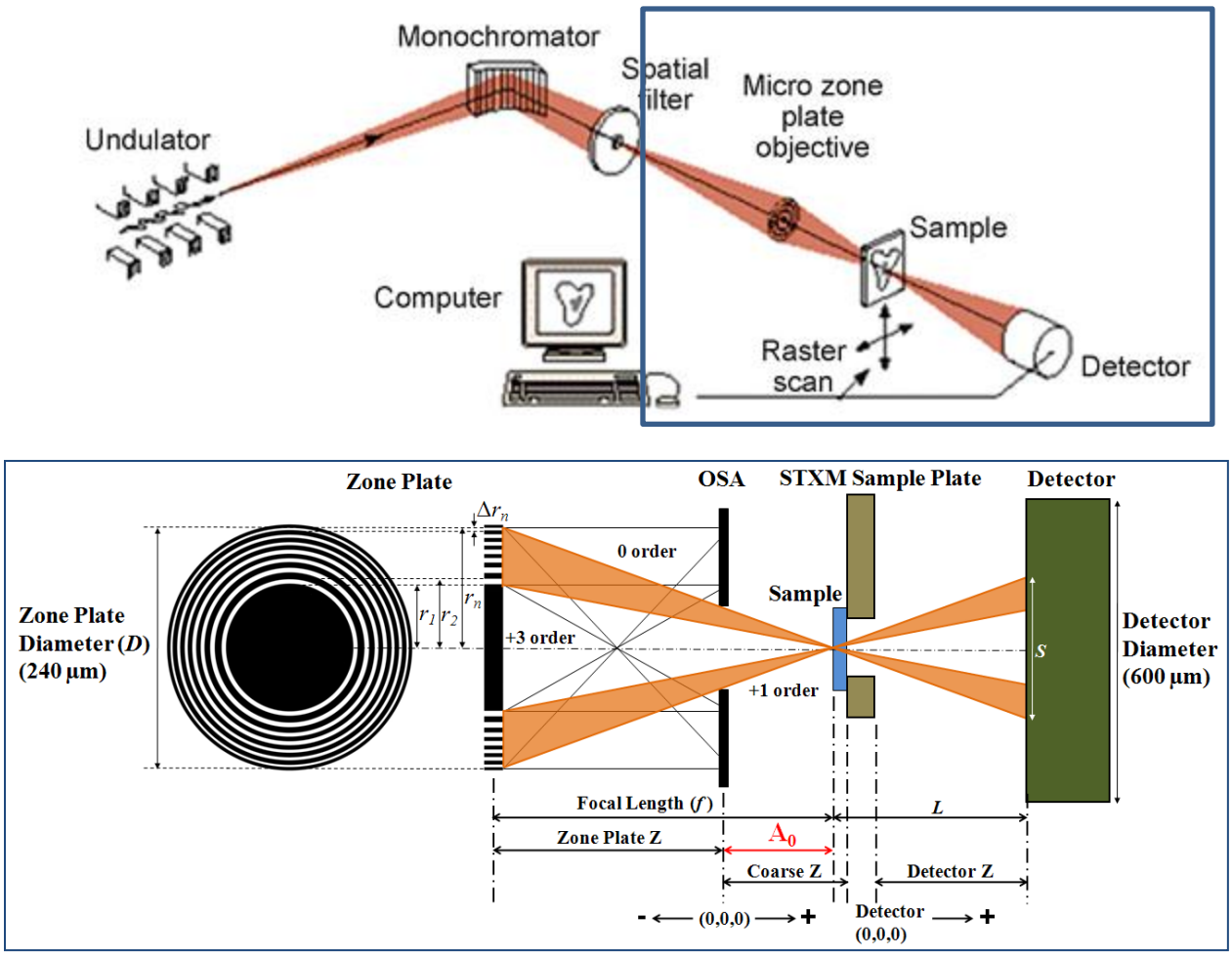

Figure 2.11 (top) Schematic diagram for the STXM microscope and (bottom) schematic diagram of order sorting aperture (OSA) in isolating the 1st order diffraction of a Fresnel zone plate present in the STXM (figure reprinted from Hitchcock *et al.*[51] with permission).

As shown in **Figure 2.11**, a monochromatic X-ray produced from the monochromator is focused to the smallest possible spot size in a STXM microscope. The transmitted intensity of the X-ray passing through the sample is monitored as a function of the sample position.

In this process, the energy resolution is governed by the monochromator in the beam line and spatial resolution is determined by the spot size of the X-rays. Hence, a zone plate, which is a circular transmission diffraction grating, creates a focused beam and that is used to obtain a small X-ray spot with good spatial resolution. Furthermore, the focal spot is determined by the width of the outermost zone of the zone plate (**Figure 2.11** right). The focal length of the zone plate lens is dependent on the X-ray energy.[52]

The zone plate is used to create a small focused X-ray spot, and a small pinhole is placed between the zone plate and sample to remove unwanted higher order diffraction. This allows the first order X-rays to pass to the sample (**Figure 2.11** right). This pinhole is named the Order Sorting Aperture (OSA) and is required to produce good quality images and spectra. Finally, the sample, which is mounted on the piezo-driven nano scanner stage, is raster scanned across the X-ray focus while detecting the transmitted X-ray by using a photon counter.[51,53] The transmitted X-rays are converted to visible photons by the phosphorous screen and then those photons are detected by a photomultiplier. The samples used in these experiments were usually ~100 nm in thickness, and deposited on the Si_3N_4 window or Transmission Electron Microscope (TEM) grids.[53] Furthermore, the STXM at the CLS can work under vacuum (100 mTorr) or a helium environment.

2.4.2.2 Rotatable Sample Holder

A rotatable sample plate was used in an experiment to verify the nature of the X-ray polarization. The azimuthal rotational sample plate used in the STXM is shown in **Figure 2.12**. This is software controlled sample holder can rotate the sample to any angle. The holder is composed of a support base and rotatable ring which connect to the power supply and is operated remotely.

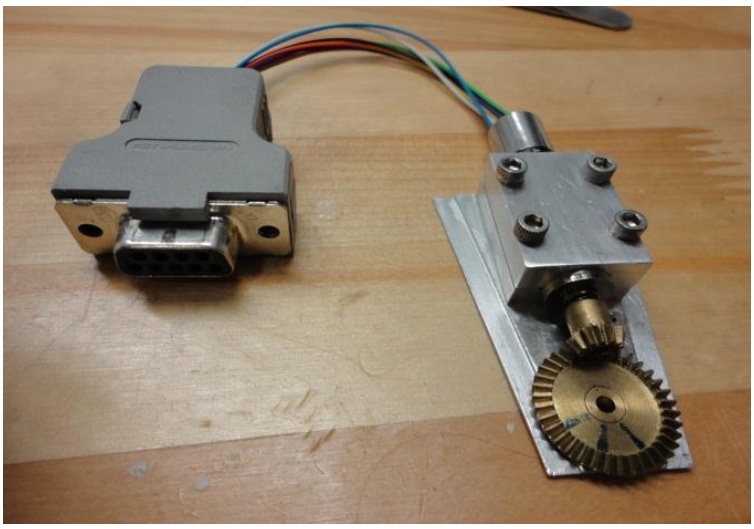

Figure 2.12 Rotatable STXM sample holder.

2.4.3 Near Edge X-ray Absorption Fine Structure (NEXAFS) Spectroscopy

X-ray transmission images and NEXAFS spectra can be obtained from the STXM. In order to record as image at a specific energy, the transmitted X-rays are recorded as a function of sample position by scanning the sample in the focal plane. Point scans, line scans and image scans are the three ways which NEXAFS spectra can be obtained. In a point scan, spectra are obtained directly by focusing on a spot on the sample and scanning the monochromator across the absorption edge. NEXAFS spectra can also be acquired using a line scan and an image scan. In line scan, X-ray photons are scanned on a line across an area of interest in the sample.

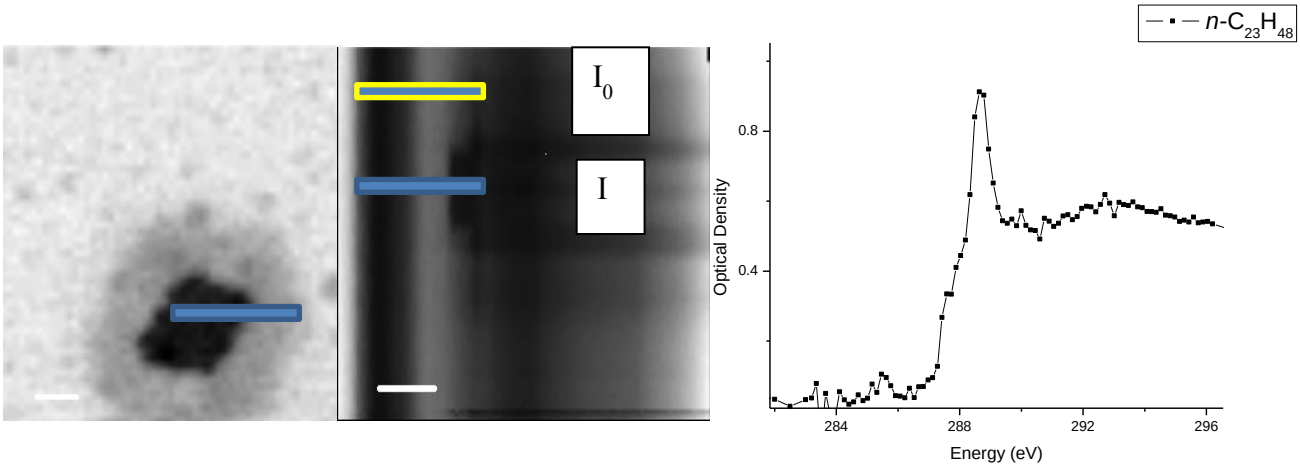

Figure 2.13 (left) STXM image recorded at 300 eV of *n*-tricosane ($C_{23}H_{48}$) crystal deposited on a 100 nm Si_3N_4 window. (middle) Line scan image (energy vs position) based on the line defined in the left image. (right) carbon 1s NEXAFS spectrum obtained from the line scan.

Figure 2.13 shows how a spectrum can obtained from a line scan. In general, the line should cover part of the sample and an open area in the NEXAFS image (blue line in the left image). Then, the energy is scanned over the absorption edge. In the case of *n*-alkanes, the energy range is usually 280 - 320 eV. The transmission intensity of the sample (I) and transmission intensity of the empty area (I_0) is integrated in the line scan image (middle) and converted to optical density (OD) and a NEXAFS spectrum is obtained (Right side image).

In the image sequence scan, a series of images are taken over the X-ray energy range. A spectra are obtained by integrating the signals coming from different areas of the images as a function of X-ray energies.[54] This is illustrated in **Figure 2.14**.

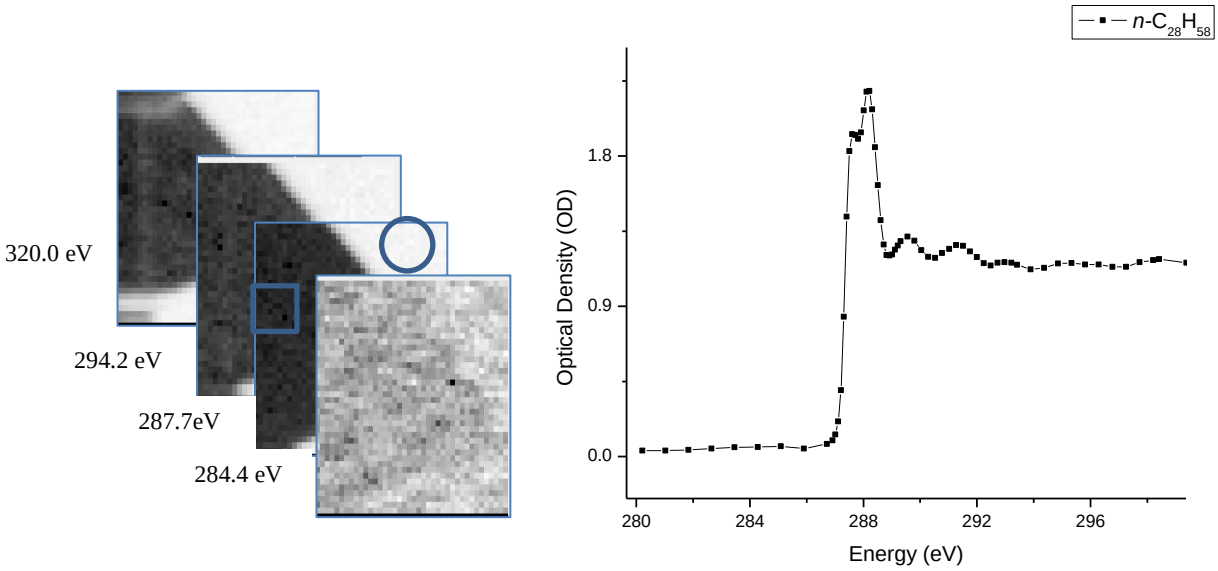

Figure 2.14 (left) a series of *n*-octacosane ($C_{28}H_{58}$) images (image scan) are taken at different energies. (right) Carbon 1s NEXAFS spectrum obtained from the square area.

Figure 2.14 presents a series of images are taken from an *n*-octacosane ($C_{28}H_{58}$) sample. The images in the left hand side were recorded at different X-ray energies which represent the pre edge region (~284.4 eV), the carbon 1s $\rightarrow \sigma^*_{C\text{-}H}$ transition (~287.7 eV), the carbon 1s $\rightarrow \sigma^*_{C\text{-}C}$ transition (~294.2 eV) and the carbon 1s $\rightarrow$ continuum (~320.0 eV). The marked circle area is an open area which is used to obtain I_0 spectrum. The square area is used to obtain the transmission spectrum (I) which is visualized in the image at 287.7 eV. The carbon 1s NEXAFS spectrum obtained from the square area is presented in the right side image in **Figure 2.14**. The NEXAFS spectra and the images are processed using aXis 2000 and Origin 7.5 programmes.[55,56]

In NEXAFS spectroscopy, radiation damage is a significant issue to consider, especially in radiation sensitive samples like *n*-alkanes. If the sample is damaged by radiation, then the NEXAFS spectra extracted from that sample might not be trustworthy. Therefore identifying the optimum conditions to obtain quality carbon 1s NEXAFS spectra is very important.

2.4.3.1 Effect of Radiation Damage in the NEXAFS Spectra of *n*-Alkanes

Radiation sensitivity of the *n*-alkanes generally increased for shorter chain length *n*-alkanes. In the process of identifying the optimum conditions for quality carbon 1s NEXAFS spectra, different scanning modes defined in §2.4.3 were performed for the same *n*-alkane. Sample spectra are shown in **Figure 2.15**, below.

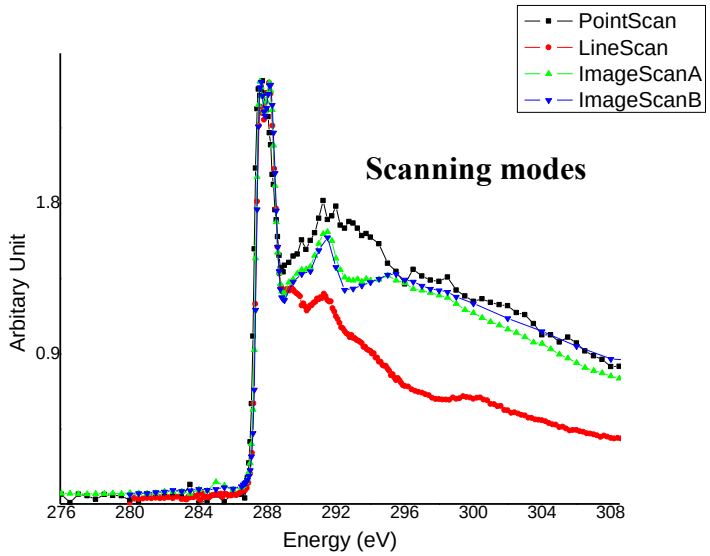

Figure 2.15 Carbon 1s NEXAFS spectra of *n*-tricosane ($C_{23}H_{48}$) (rescaled) with different scanning modes.

The effect of radiation damage can be identified in two ways. One is to identify the intensity of the peak which results due to radiation damage. In *n*-alkanes; single carbon-carbon bonds can be converted into a carbon-carbon double bond by radiation damage. This can be found from the intensity of the peak around 285 eV (carbon 1s $\rightarrow \pi^*_{C=C}$ transition). The other way to identify radiation damage is through mass loss. This can be found by observing how intensity of the spectra decreases at higher energies, as the continuum is proportional to sample thickness. The carbon 1s NEXAFS spectra of *n*-tricosane ($C_{23}H_{48}$) obtained from a line scan with a 200 nm defocused X-ray and 500 nm defocused X-ray spot typically gave a radiation damage π^* feature

at 285 eV region with significant intensity. In a defocused scan, the X-ray spot size was increased. The continuum intensity of the line and point scan spectra are lower, indicating significant mass loss. In contrast, the carbon 1s NEXAFS spectra of *n*-tricosane ($C_{23}H_{48}$) obtained by image scan did not show a π^* transition around the 285 eV region. The spectrum obtained from 125 nm X-ray defocus (image scan B) showed less mass loss than the spectrum obtained by 100 nm X-ray defocus image scan (image scan A). Therefore, in this experiment, a larger (125 nm defocus) X-ray image scan with a low scanning time was the compromise suitable scanning mode to obtain good quality spectra of *n*-tricosane ($C_{23}H_{48}$) and other *n*-alkane crystals.

The stability in the monochromator energy scale is important for reliable NEXAFS spectra. Therefore, the energy scale of the carbon 1s NEXAFS spectra of each *n*-alkane must be calibrated and verified.

2.4.3.2 Calibration of the Monochromator Energy Scale

The monochromator energy scale was calibrated with CO_2 gas (~ 3torr). This energy calibration was done by introducing CO_2 (~ 3 torr) gas in to the STXM chamber while the sample is inside the chamber. In the process, both the CO_2 and the sample spectra could be obtained simultaneously. The absorption feature corresponding to the carbon 1s $\rightarrow$ 3s (v=0) transition of CO_2 was identified. Once identified, its energy was compared with the available literature value of 292.74 eV for this transition[21] and the shift in energy scale for calibration was determined. With that shift, the energy scale of the sample spectra was corrected.

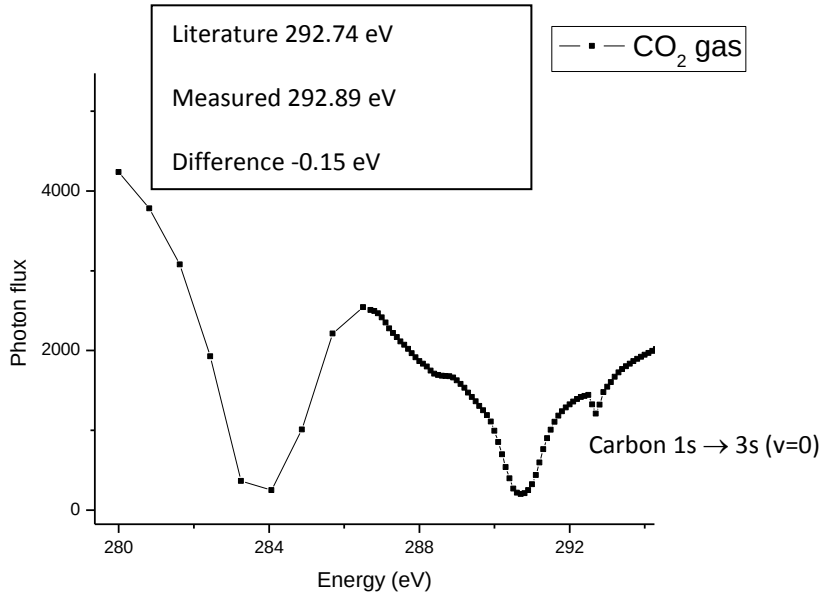

Figure 2.16 Carbon 1s spectrum of CO_2 gas, in transmission.

3. Results and Discussion

3.1 Optical Microscopy Measurements

The shape of the *n*-alkane crystals prepared in this project were initially identified using the Olympus BX 51 and Nikon eclipse ME600 optical microscopes at the CLS and Chemistry Department, University of Saskatchewan, respectively. All the polarized Optical Microscope (OM) images were taken under bright field illumination. The optical microscopy images were taken in two conditions. First, the morphology of the *n*-alkane crystals was taken at room temperature. This will be discussed in §3.1.1. Secondly, the *n*-alkane crystals were heated to near their melting point and the change in the morphology was observed throughout the order-disorder transitions. This is explained in §3.1.2.

3.1.1 The Morphology of Different *n*-Alkane Crystals at Room Temperature

N-alkane crystals were obtained using a solution casting method. In the solution casting method, an ideal solvent must be identified to obtain well-ordered single *n*-alkane crystals. Part of this project involved optimizing sample preparation conditions by trial and error. These sample preparation and optimization results are presented here.

Sample Preparation

Various factors must be considered in the process of the sample preparation of *n*-alkanes. Suitable solvent in each *n*-alkanes, temperature of the system, thickness of the substrate are some of the main factors. A detailed discussion on the process of the sample preparation of *n*-alkanes will be described below. In this discussion, it was found that the morphology of the crystals of the long *n*-alkane chains, *n*-tetracontane ($C_{40}H_{82}$) and *n*-octacosane ($C_{28}H_{58}$) remain stable at room temperature. Furthermore, the morphology of those two *n*-alkanes did not vary with the

nature of the substrate. The short *n*-alkanes chains, *n*-tricosane ($C_{23}H_{48}$) and *n*-tetracosane ($C_{24}H_{50}$) showed some dependency towards substrate selection, and were unstable if stored at room temperature.

Systematic Identification of the Suitable Solvent in *n*-Alkanes

Identification of a suitable solvent is very important to obtain a well-ordered *n*-alkane single crystal. Zou *et al.*[41] were successful in preparing single crystals of *n*-tetracontane ($C_{40}H_{82}$) and *n*-nonadecane ($C_{19}H_{40}$) by solution casting.[41] They dissolved *n*-tetracontane ($C_{40}H_{82}$) in toluene and *n*-nonadecane ($C_{19}H_{40}$) in acetonitrile with a mass/volume ratio of 0.5 mg/ml and at a temperature of 50 °C. A drop of each solution was placed onto a 100 nm thick Si_3N_4 window. For *n*-tetracontane ($C_{40}H_{82}$), the crystallization was performed by evaporating the solvent at room temperature, but for *n*-nonadecane ($C_{19}H_{40}$), the solution was cast at 8 °C.[41]

In his work, well-ordered thin *n*-tetracontane ($C_{40}H_{82}$) crystals were obtained from the rapid evaporation of toluene. Different evaporation techniques were studied in order to identify the best crystallization conditions. In the process, the solvent was evaporated rapidly by pouring the solution on the substrate, by evaporating the solvent with a flow of gas gun, and by naturally evaporating the solvent at room temperature. The latter evaporation technique was found as the best way to obtain well-ordered diamond shaped crystals. This method was used to evaporate the solvent in all four *n*-alkanes.

3.1.1.1 *n*-tetracontane ($C_{40}H_{82}$)

As mentioned by Zou *et al.*,[41] toluene as a suitable solvent for *n*-tetracontane ($C_{40}H_{82}$) for this work. *N*-tetracontane ($C_{40}H_{82}$) was dissolved in toluene with a mass/volume ratio of 1.0 mg/2.0 ml and stirred at 50 °C. A drop of the solution was placed in the silicon nitride (Si_3N_4) coated

wafer and was allowed to evaporate rapidly at room temperature. This, procedure was repeated with the different mass/volume ratios such as 2:1, 1:3 and 1:4.

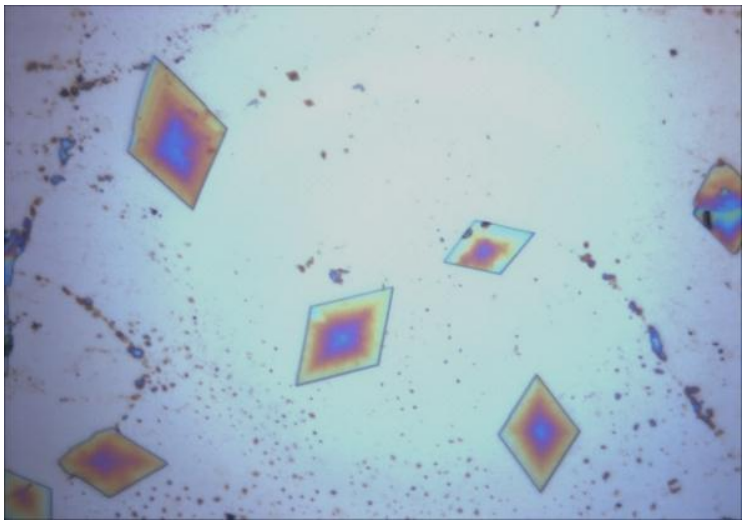

Figure 3.1 Polarized optical microscopy images of *n*-tetracontane ($C_{40}H_{82}$) crystals cast from the toluene solution with the mass/volume ratio 1.0 mg/2.0 ml (50X objective magnification).

Only the 1:2 (mass of *n*-alkane/volume of solvent) ratio gave well-ordered diamond shape *n*-tetracontane ($C_{40}H_{82}$) crystals (**Figure 3.1**). Therefore, all solutions prepared subsequently used the mass/volume ratio of 1.0 mg/2.0 ml.

Further, Zou *et al.*[41] prepared well-ordered diamond shape *n*-nonadecane ($C_{19}H_{40}$) crystals from acetonitrile solution with the same mass/volume ratio, at 8 °C. On this basis, the solvent and temperature are varied to find the best conditions. Zou *et al.*[41] used more polar acetonitrile to dissolve the short *n*-nonadecane ($C_{19}H_{40}$) chain and less polar acetone to dissolve long *n*-tetracontane ($C_{40}H_{82}$) chain. This polarity trend guides the following work.

3.1.1.2 *n*-tricosane ($C_{23}H_{48}$) and *n*-tetracosane ($C_{24}H_{50}$)

A set of different solvents with polarity indexes close to acetonitrile were used systematically to identify the most suitable solvent for the shorter chain *n*-alkanes, *n*-tricosane ($C_{23}H_{48}$) and *n*-

tetracosane ($C_{24}H_{50}$). The polarity index of a solvent is a relative measure of the degree of interaction of the solvent with various polar test solutes. As *n*-tricosane ($C_{23}H_{48}$) is one carbon shorter than *n*-tetracosane ($C_{24}H_{50}$), the same set of solvents (acetone, ethanol, acetonitrile and methanol) were tested. As predicted, both *n*-alkanes responded in the same way towards these solvents. Both gave poor crystals when cast from acetone, ethanol and toluene.

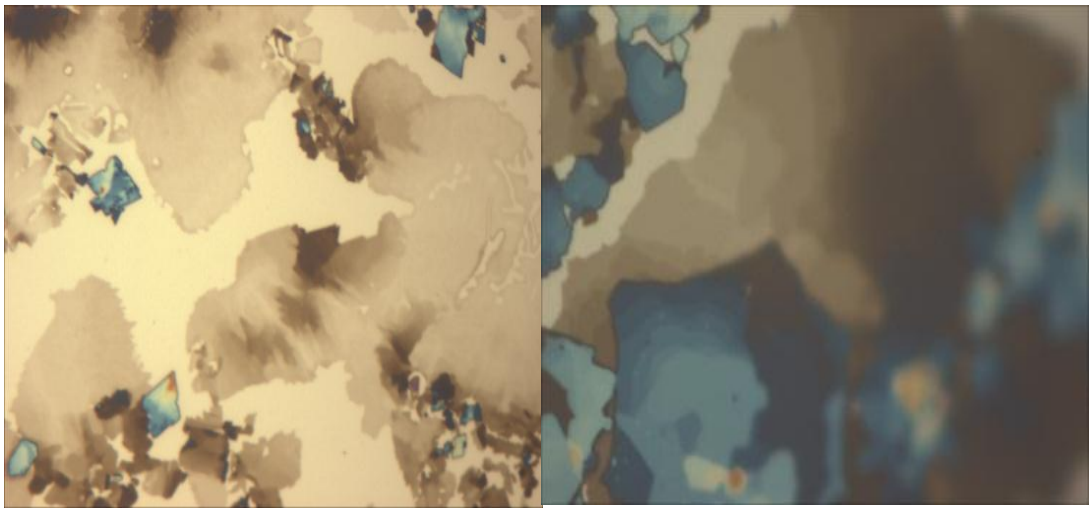

Figure 3.2 Polarized optical microscopy images of *n*-tricosane ($C_{23}H_{48}$) crystals deposited from (left) an acetone and (right) ethanol solution at room temperature (50X objective magnification).

Figure 3.2 shows that the *n*-tricosane ($C_{23}H_{48}$) crystals obtained from acetone (left) and ethanol (right) solution. Well-ordered diamond shape crystals were not observed. A similar observation was observed with toluene. Therefore, more polar acetonitrile and methanol solvents were then examined.

Figure 3.3 Polarized optical microscopy images of *n*-tricosane ($C_{23}H_{48}$) crystals deposited from (left) acetonitrile and (right) methanol solution at room temperature (50X objective magnification).

N-tricosane ($C_{23}H_{48}$) crystals obtained from acetonitrile (**Figure 3.3** left) and methanol (**Figure 3.3** right) have a better morphology when compared to the morphology of the *n*-tricosane ($C_{23}H_{48}$) crystals obtained from acetone and ethanol. However, the edges of most of the crystals obtained from these two solutions are distorted. The amount of distortion in the short chain *n*-alkane (*n*-tricosane ($C_{23}H_{48}$) and *n*-tetracosane ($C_{24}H_{50}$)) crystal morphology increases with the time that sample remains at room temperature. Hence, the observations show that the morphology of the shorter chain *n*-alkanes *n*-tricosane ($C_{23}H_{48}$) and *n*-tetracosane ($C_{24}H_{50}$) are not stable at room temperature. Furthermore the observations obtained from acetonitrile were not reproducible. Therefore *n*-tricosane ($C_{23}H_{48}$) and *n*-tetracosane ($C_{24}H_{50}$) crystals were deposited from methanol solutions at 8 °C and stored in the refrigerator.

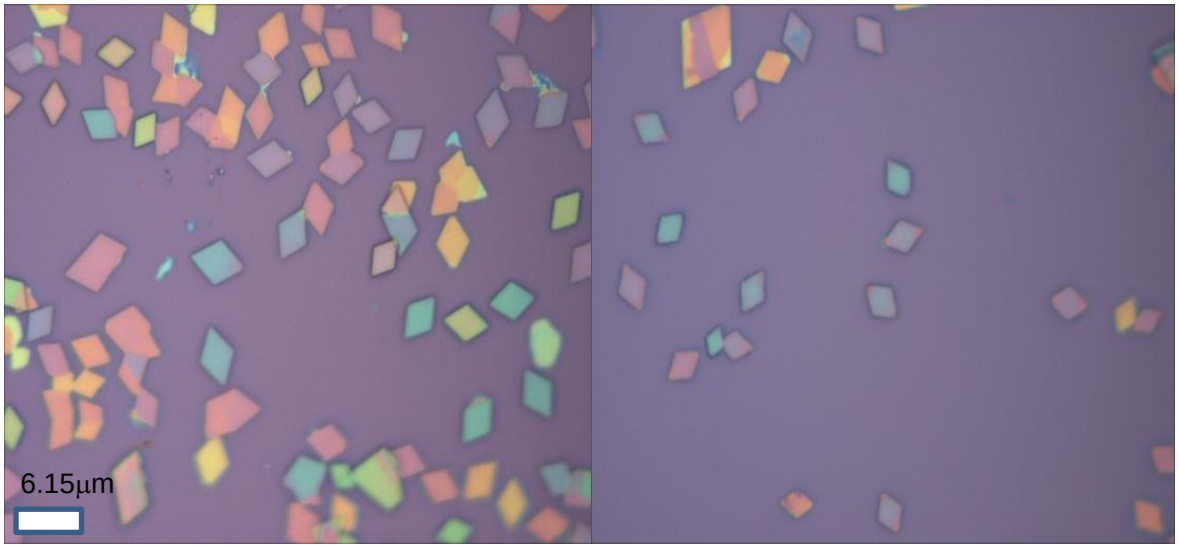

Figure 3.4 Polarized optical microscopy images of (left) *n*-tricosane ($C_{23}H_{48}$) crystals and (right) *n*-tetracosane ($C_{24}H_{50}$) crystals deposited from methanol solution at room temperature (50X objective magnification).

Well-ordered diamond shape *n*-tricosane ($C_{23}H_{48}$) and *n*-tetracosane ($C_{24}H_{50}$) crystals were obtained when deposited from methanol solution inside the refrigerator (~ 8 °C) (**Figure 3.4**). Furthermore, the crystals in **Figure 3.4** have a wide range of colour and size. Here, the colour of the crystal depends on the thickness of the crystals, as the different interference effects from the different thickness of the crystal will change visible light absorption.

For the optical microscopy measurements, samples were prepared on Si_3N_4 coated wafers. Wafers gave well-ordered diamond morphology *n*-tricosane ($C_{23}H_{48}$) and *n*-tetracosane ($C_{24}H_{50}$) crystals as shown in **Figure 3.4**. These wafers could not be used for the STXM transmission measurements and a thick support cannot be used. For STXM, the sample and substrate should be thin enough (~ 100 nm) to allow the X-ray beam to penetrate. Therefore, *n*-alkane samples were prepared on 100 nm thick Si_3N_4 windows.

Surprisingly, for short *n*-alkane chain *n*-tricosane ($C_{23}H_{48}$) and *n*-tetracosane ($C_{24}H_{50}$) the morphology of the crystals was distorted when it was deposited on the Si_3N_4 window. Therefore

silicon monoxide (Sigma-Aldrich 99%) (SiO) layer was deposited on top of the Si_3N_4 window by physical vapor deposition, to mimic the native oxide surface conditions.

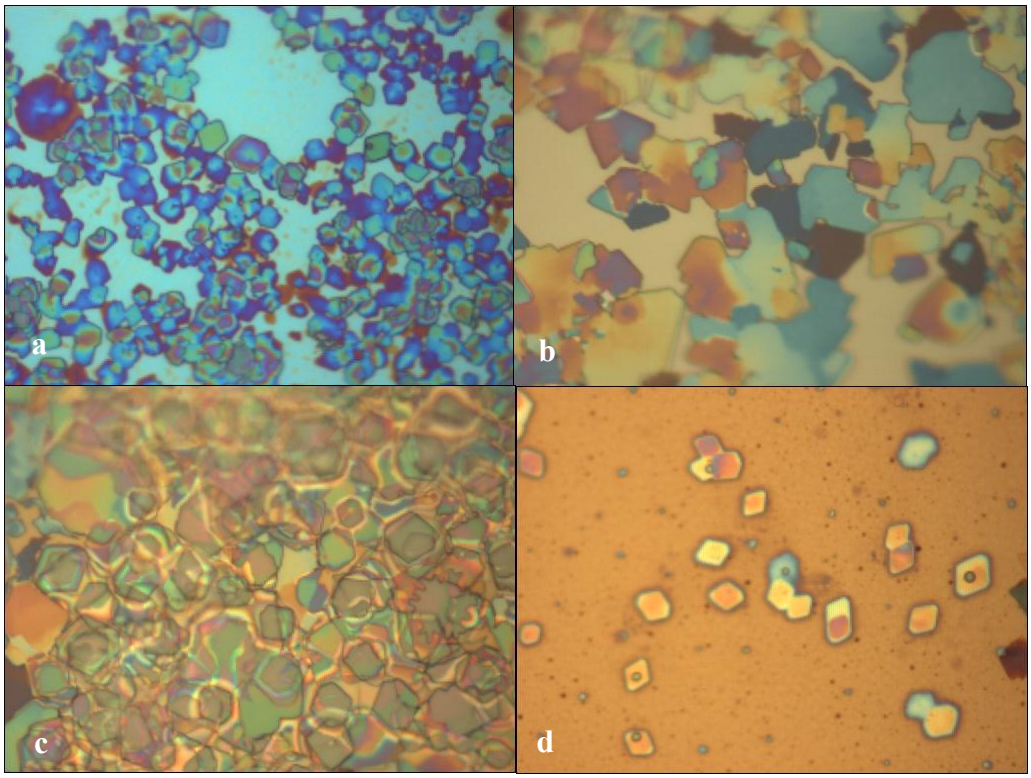

Figure 3.5 Polarized optical microscopy images of *n*-tricosane ($C_{23}H_{48}$) crystals deposited on a a) Si_3N_4 window, b) Si_3N_4 window coated with a 10 nm SiO layer, c) Si_3N_4 window coated with a 20 nm SiO layer and d) Si_3N_4 window coated with a 30 nm SiO layer at room temperature (50X objective magnification).

Figure 3.5 shows that the morphology of the *n*-tricosane ($C_{23}H_{48}$) crystals improves with the thickness of the SiO layer. The best morphology of the *n*-tricosane ($C_{23}H_{48}$) and the *n*-tetracosane ($C_{24}H_{50}$) crystal was observed when a 30 nm SiO layer was deposited on the Si_3N_4 window. This ideal thickness of SiO on Si_3N_4 window was used for the subsequent STXM sample preparation.

3.1.1.3 *n*-octacosane ($C_{28}H_{58}$)

The chain length of *n*-octacosane ($C_{28}H_{58}$) lies in between *n*-tetracontane ($C_{40}H_{82}$) and *n*-tricosane ($C_{23}H_{48}$), so a suitable solvent for this *n*-alkane should have a moderate polarity index value, between that of toluene and methanol. Keeping that idea in mind, toluene, benzene, dichloromethane, chloroform, methanol, *n*-butanol and isopropyl alcohol were tested to identify the best solvent for *n*-octacosane ($C_{28}H_{58}$).

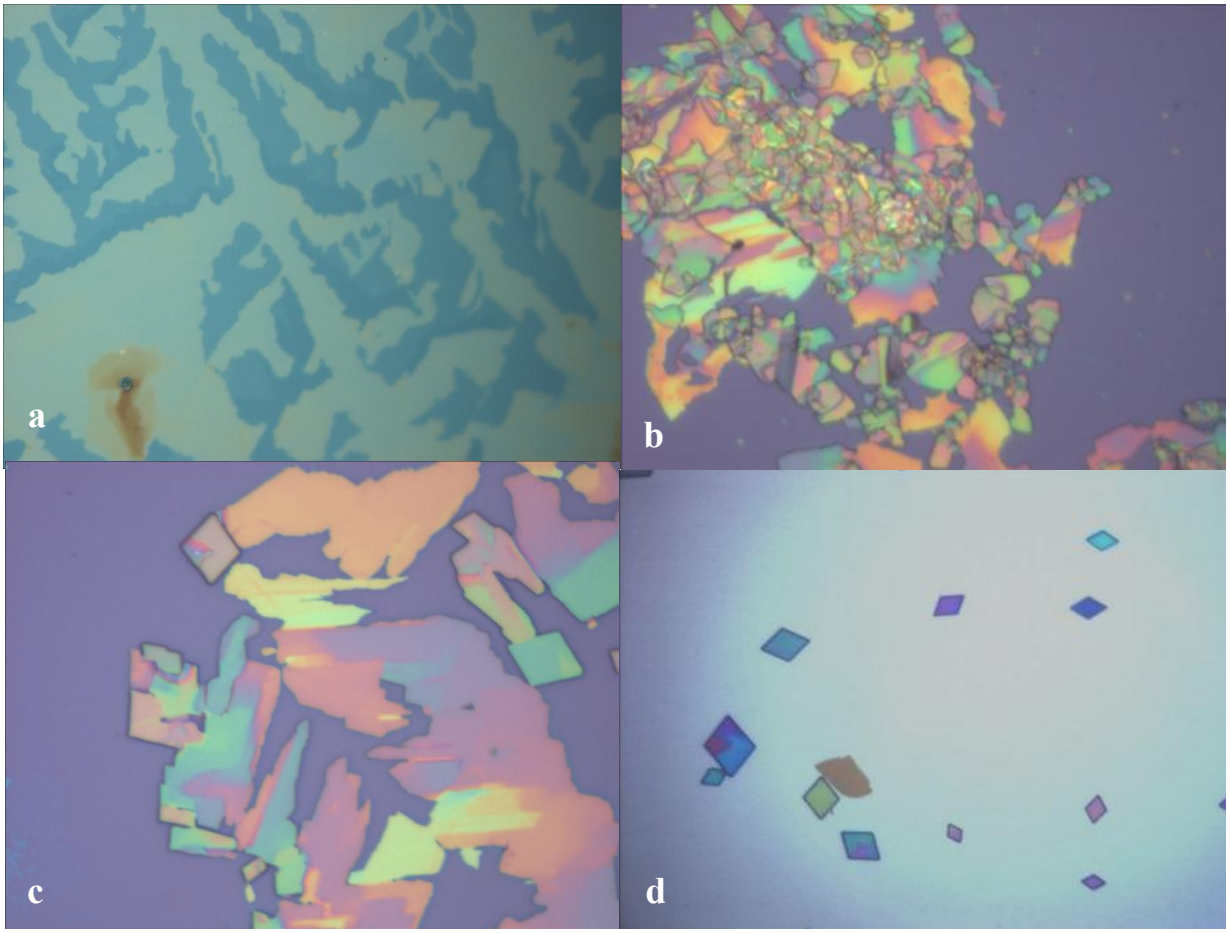

Figure 3.6 Polarized optical microscopy images of *n*-octacosane ($C_{28}H_{58}$) crystals deposited from a) toluene solution, b) methanol solution, c) *n*-butanol solution and d) isopropyl alcohol solution at room temperature (50X objective magnification).

The morphology of the *n*-octacosane ($C_{28}H_{58}$) crystals deposited from toluene solution (**Figure 3.6a**) did not give a diamond shape. This observation was also seen for benzene, dichloromethane and chloroform solvents.

Methanol was used to obtain better *n*-octacosane ($C_{28}H_{58}$) crystals. **Figure 3.6b** shows that the shape of the *n*-octacosane ($C_{28}H_{58}$) crystal is better when cast from methanol solution. However, the morphology of the *n*-octacosane ($C_{28}H_{58}$) was not a well-ordered diamond shape. Next, moderately polar *n*-butanol and isopropyl alcohol were used to obtained *n*-octacosane ($C_{28}H_{58}$) crystals. As shown in **Figure 3.6c**, *n*-butanol gave well-ordered diamond shape crystals. This observation was not reproducible, and only few crystals were obtained from this solvent.

Finally, the solvent was changed in to the isopropyl alcohol and the morphology of the *n*-octacosane ($C_{28}H_{58}$) crystals obtained from this solvent was good (**Figure 3.6d**). Further, this observation was reproducible, and many crystals were deposited on the substrate. The optimum condition used in depositing each *n*-alkane on the Si_3N_4 window is summarized in **Table 3.1.**

Table 3.1 Summary of the sample preparation procedures for *n*-alkane crystals.

***n*-alkane**	**Sample preparation**			
	Solution concentration	**Solution temperature**	**Substrate**	**Evaporation technique**
n-tricosane ($C_{23}H_{48}$)	1.0 mg/2.0 ml	Solution heated up to the 50°C and cooled to room temperature	100 nm Si_3N_4 window with 30 nm SiO layer.	Evaporation in the refrigerator
n-tetracosane ($C_{24}H_{50}$)	1.0 mg/2.0 ml	Solution heated up to the 50°C and cooled to room temperature	100 nm Si_3N_4 window with 30 nm SiO layer	Evaporation in the refrigerator
n-octacosane ($C_{28}H_{58}$)	1.0 mg/2.0 ml	Solution heated up to the 50°C and cooled to room temperature	100 nm Si_3N_4 window	Rapid evaporation at room temperature
n-tetracontane ($C_{40}H_{82}$)	1.0 mg/2.0 ml	Solution heated up to the 50°C and cooled to room temperature	100 nm Si_3N_4 window	Rapid evaporation at room temperature

3.1.2 Variations in the Morphology of Different *n*-Alkane Crystals with Temperature

This section will describe optical microscopy measurements to study the morphology variation on *n*-alkanes through the order-disorder transitions.

3.1.2.1 *n*-tetracontane ($C_{40}H_{82}$)

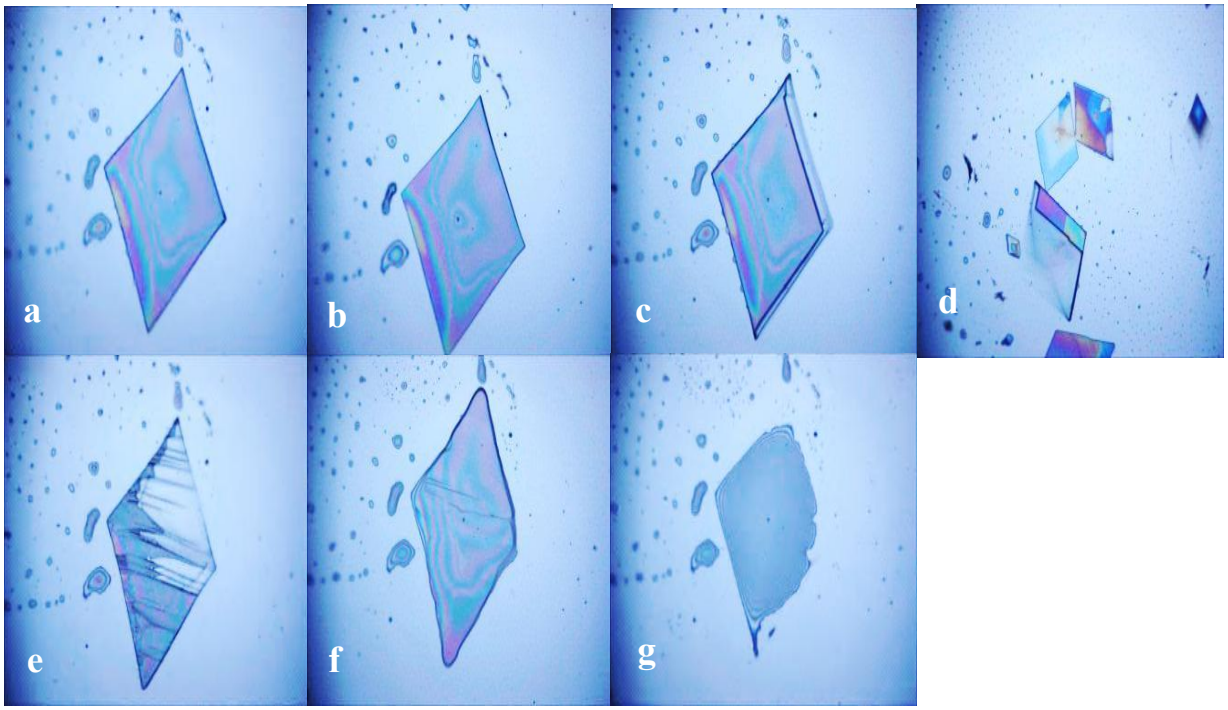

Figure 3.7 Polarized optical microscopy images of *n*-tetracontane single crystals ($C_{40}H_{82}$) at a) 25.4 °C (R.T), b) 60.0 °C, c) 73.2 °C, d) 74.1 - 74.5 °C, e) 75.0 °C, f) 82.0 °C, g) 82.5 - 82.8 °C (50X objective magnification).

Figure 3.7 shows how the morphology of the *n*-tetracontane ($C_{40}H_{82}$) crystals varies with temperature. There was no change observed in the morphology of the *n*-tetracontane ($C_{40}H_{82}$) crystal until 73.2 °C (image a-c), but in the temperature range 73.0 - 75.0 °C, some changes are observed (image c-e). The morphology of the *n*-tetracontane ($C_{40}H_{82}$) crystal changes further around 82.0 °C (image f), and is entirely melted in the temperature range of 82.5 - 82.8 °C (image g). The melting point of *n*-tetracontane ($C_{40}H_{82}$) is 80.85 °C.[40,42]

3.1.2.2 *n*-octacosane ($C_{28}H_{58}$)

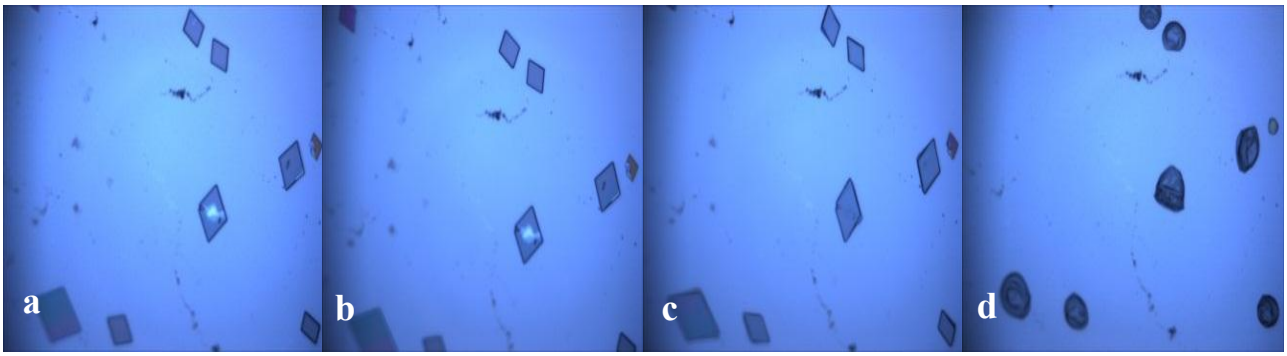

Figure 3.8 Polarized optical microscopy images of the *n*-octacosane single crystals ($C_{28}H_{58}$) at a) 25.4 °C (R.T), b) 50.0 °C, c) 58.7 - 59.3 °C, d) 62.2 °C (50X objective magnification).

Similarly, **Figure 3.8** shows the variation of the morphology of *n*-octacosane ($C_{28}H_{58}$) crystals with temperature. The morphology of the *n*-octacosane ($C_{28}H_{58}$) crystals remains the same up to the temperature 58.7 °C (image a-b), but the sample showed some morphology change in the temperature range of 58.7-59.3 °C (image c). The crystals melted around 62.2 °C (image d). The melting point of *n*-octacosane ($C_{28}H_{58}$) is 60.97-61.05 °C.[36,42]

3.1.2.3 *n*-tricosane ($C_{23}H_{48}$) and *n*-tetracosane ($C_{24}H_{50}$)

Unlike *n*-tetracontane ($C_{40}H_{82}$) and *n*-octacosane ($C_{28}H_{58}$), the short chain *n*-alkanes, *n*-tricosane ($C_{23}H_{48}$) and *n*-tetracosane ($C_{24}H_{50}$) did not show any structural changes before their melting point in the optical microscope. All crystals suddenly melted at their melting point.

Discussion

During the heating process of the *n*-tetracontane ($C_{40}H_{82}$) crystals, the morphology of the crystal changed in the temperature range of 73.0 – 75.0 °C. This observation was supported by the differential scanning calorimeter (DSC) spectra obtained in this project. DSC showed a peak around 74.92 °C, which may reflect this change (**Table 2.1**). Further Wang *et al.*[40] mentioned a solid-solid transition of the *n*-tetracontane ($C_{40}H_{82}$) crystal at 74.55 °C (**Table 1.1** and **2.1**),

named as a transition from M phase (low temperature phase or mesophase) to the C phase (an intermediate form between crystalline phase and liquid phase).[40] Also they mentioned that during the heating process, the rotator or disorder phase was not observed for *n*-tetracontane ($C_{40}H_{82}$) crystals. In this project, some change in the morphology was observed for the *n*-tetracontane ($C_{40}H_{82}$) crystal around 82.0 °C from optical microscope measurements. Dirand *et al.*[42] mentioned that an order-disorder transition occurs at 80.35 °C (**Table 1.1**).[42]

Similarly from the optical microscope, the morphology of the *n*-octacosane ($C_{28}H_{58}$) crystal changed in the temperature range of 58.7 - 59.3 °C. This range is close to the value of the order-disorder transition obtained from DSC measurements (**Table 2.1**). Further, Dirand *et al.*[42] has mentioned the structure corresponding for that particular disorder phase was triclinic RIII, which has a disorder orientation along the long c axis with non-planar defects.[42]

Even though there was no morphology change observed before their melting point for the *n*-tricosane ($C_{23}H_{48}$) and *n*-tetracosane ($C_{24}H_{50}$) crystals, different kinds of order-order, order-disorder and disorder-disorder transitions were reported in the literature.[42,36,38] This is summarized in the **Table 1.1**. Most of the literature DSC studies identified the order-disorder transitions of *n*-tricosane ($C_{23}H_{48}$) and *n*-tetracosane ($C_{24}H_{50}$), but only some could identify both order-disorder and disorder-disorder transitions for a particular *n*-alkane. Furthermore, Dirand *et al*.[42] reported the structure exists in the ordered (crystalline phase) and disordered (rotator) phase in *n*-tricosane ($C_{23}H_{48}$) and *n*-tetracosane ($C_{24}H_{50}$).[42]

Dirand *et al.*[42] also reported that an order-order (crystal-crystal) transition was observed for *n*-tricosane alkane ($C_{23}H_{48}$), and this will change the orthorhombic crystal structure of *n*-tricosane ($C_{23}H_{48}$) in to a new form of orthorhombic crystal structure with a different space group

(Pbnm).[31] Furthermore, in the order-disorder transition of *n*-tricosane ($C_{23}H_{48}$), a disordered structure corresponds to the orthorhombic β form which has a face centered space group Fmmm.[42]

Unlike odd *n*-alkanes, the even length *n*-alkanes did not show order-order phase transitions and shows only order-disorder transitions.[42] Dirand *et al.*[42] has mentioned a disorder phase structure in the *n*-tetracosane ($C_{24}H_{50}$), corresponds to the rhombohedral α-RIII form with a space group of R3m. [42] In this structure, the stacking mode of the molecular layers correspond to the ABC rhombohedral sequence, where molecules likely have rotation around their c axis.[42]

On the basis of these results and the literature, it is concluded that an optical microscope is likely not sensitive to the structural changes as associated with order-disorder transitions in *n*-tricosane ($C_{23}H_{48}$) and *n*-tetracosane ($C_{24}H_{50}$) crystals.

3.2 NEXAFS Spectra of *n*-Alkanes with Different Crystal Structures from Different Chain Lengths

This section will show the changes observed in the carbon 1s NEXAFS spectra of *n*-alkanes with different crystal structures, which are varied by using different chain lengths at room temperature. The main goal in this project is to identify the "matrix effects" in the carbon 1s NEXAFS spectroscopy of *n*-alkanes. Hence, experiments conditions were optimized in the way that eliminates other effects such as orientational effects.

NEXAFS spectroscopy measurements of *n*-alkanes, as a function of chain length at room temperature, were initially performed by using left circular polarization in order to avoid orientation effects. In left circularly polarized radiation, the electric field vector of the X-ray precesses in the sample plane, and therefore in-plane orientation effects should cancel out.

3.2.1 Carbon 1s NEXAFS Spectra Obtained with Left Circular Polarized Radiation

This section will present the carbon 1s NEXAFS spectra of *n*-alkanes recorded with left circularly polarized radiation, in conditions where NEXAFS spectra were obtained with minimal radiation damage (see §2.4.3). All the room temperature NEXAFS spectra with the left circularly polarized radiation were taken by the image scan mode under helium environment (0.16 atm), except as indicated. All spectra were calibrated using CO_2 gas (see §2.4.3.2).

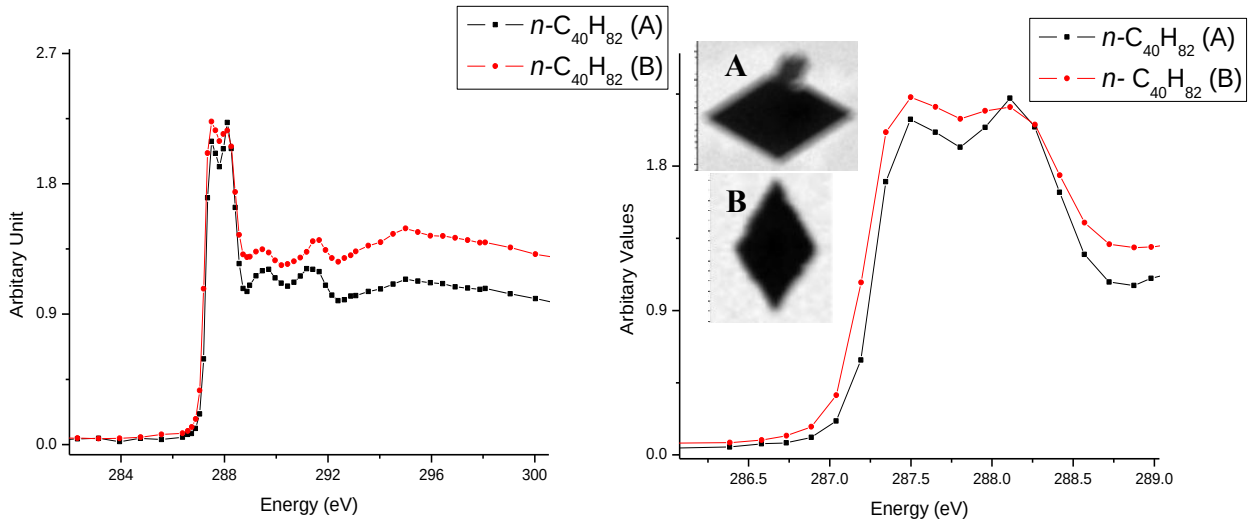

Figure 3.9 (left) NEXAFS spectra of *n*-tetracontane ($C_{40}H_{82}$) (rescaled), recorded with left circularly polarized radiation at room temperature (25.4 °C). (right) C-H energy region (287-289 eV) of the same NEXAFS spectra.

Figure 3.9 presents the NEXAFS spectra of *n*-tetracontane ($C_{40}H_{82}$) recorded with left circularly polarized radiation, at room temperature. The two spectra were obtained examining crystals of two different orientations A and B in the same *n*-tetracontane ($C_{40}H_{82}$) sample. Even though both spectra were obtained from the same *n*-alkane crystal, the shapes of the spectra are different with a change in crystal orientation as shown in **Figure 3.9**. The relative intensity of the first two peaks was not same in the two spectra. In one spectrum (right $C_{40}H_{82}$ A), the intensity of the first

peak was lower than the second peak, while in other (right $C_{40}H_{82}$ B); the intensity of the first peak was higher than the second peak.

The left circularly polarized spectra obtained for other *n*-alkanes such as *n*-tricosane ($C_{23}H_{48}$), *n*-tetracosane ($C_{24}H_{50}$) and *n*-octacosane ($C_{28}H_{58}$), also showed similar angle dependence as **Figure 3.9**. The experiment was repeated with same set of *n*-alkanes and angle dependence observed in the spectra was consistent with the **Figure 3.9**.

Discussion

Even though two spectra from the same *n*-tetracontane ($C_{40}H_{82}$) crystals in the **Figure 3.9** show a different relative intensity relationship in the two C-H peaks (287-288 eV), this observation should not happen with left circularly polarized radiation. The spectra obtained from the circular polarized radiation should not be sensitive to the in-plane orientation of the crystal. If the radiation is in fact elliptically polarized, then there will be a difference in spectra as the crystal is oriented with respect to this elliptical polarization. Therefore, we conclude that significant linear polarization "contamination" is present in this energy range, distorting the intended circular polarization to elliptical polarization. The possibility of crystal to crystal differences is examined below.

3.2.1.1 Linear Dichroism Contamination in the Left Circularly Polarized NEXAFS Spectra of *n*-Alkanes

As it was not possible to avoid linear dichroism effects, orientation effects were explicitly studied. First, differences in the aspect ratio of crystals were examined, but later, it was determined that the polarization contamination was the most significant factor.

As a next step, the purity of the circular polarization was examined by azimuthal rotation of the sample. Carbon 1s NEXAFS spectra of same *n*-alkane were recorded as a function of orientation was obtained by rotating the same single crystal. This is shown in **Figure 3.10**.

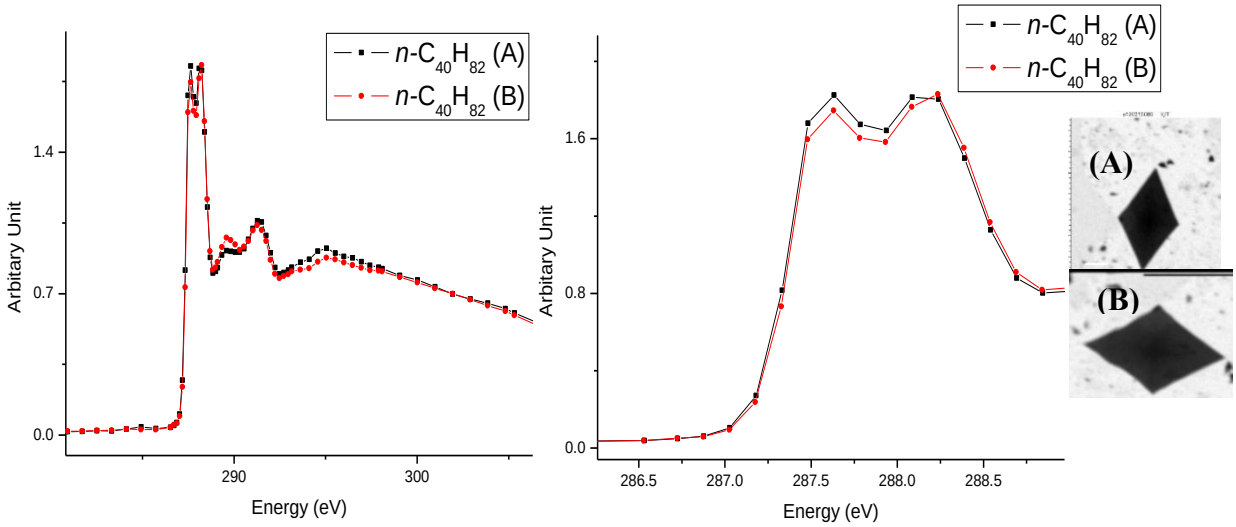

Figure 3.10 (left and middle) Carbon 1s NEXAFS spectra of *n*-tetracontane ($C_{40}H_{82}$) (rescaled) recorded with left circularly polarized radiation for different orientations of the same single crystal. (right) STXM images of the corresponding *n*-tetracontane crystal ($C_{40}H_{82}$).

Figure 3.10 presents the spectral variation of left circularly polarized carbon 1s NEXAFS spectra of *n*-tetracontane ($C_{40}H_{82}$) with respect to different crystal orientations. This was obtained by rotating the same *n*-tetracontane ($C_{40}H_{82}$) crystal in the sample. A detailed description about the rotatable sample plate was provided in §2.4.2.2. The spectral variation which was observed with sample rotation is consistent with the spectral variation in the **Figure 3.9**. Hence, it was concluded that this spectral change could only rise due to the orientation of the crystal, and that this was not due to the quality or purity of different crystals observed. Therefore, significant linear polarization "contamination" is present in this energy range (287-300 eV). As it was not possible to use circular polarized radiation to avoid linear dichroism effects, angle dependent

NEXAFS spectra were explicitly measured. The angle dependent NEXAFS spectra were measured by aligning the X-ray polarization along the principal axes (X, Y) of the crystal, as defined in **Figure 3.11**.

3.3.2 Carbon 1s NEXAFS Spectra Obtained with Inclined Linearly Polarized Radiation

The angle dependent of NEXAFS spectra were obtained by aligning the electric field vector of the inclined linearly polarized X-rays along the direction of the principal axes (X, Y) of the *n*-alkane crystal (**Figure 3.11**). The spectral behavior obtained in all *n*-alkanes in this way is presented in **Figure 3.11**.

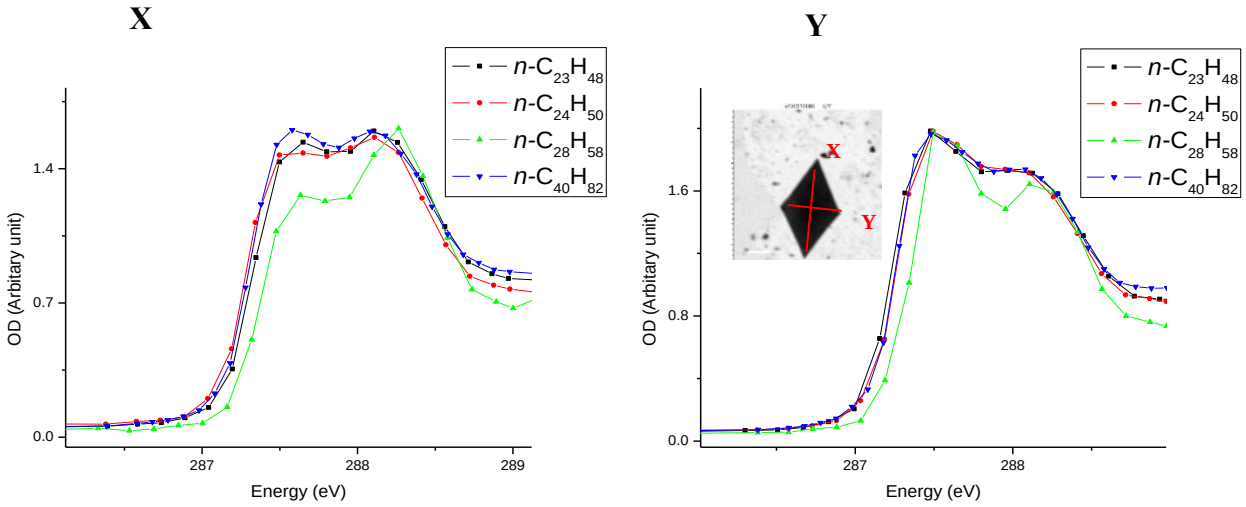

Figure 3.11 Calibrated carbon 1s NEXAFS spectra of different *n*-alkanes (rescaled), recorded with the X-ray polarization directed (left) along the X (long axis) and (right) along the Y (short axis) direction of the crystal. The relative reliability of the energy scale follows in §3.3.2.1.

According to the **Figure 3.11**, in all four *n*-alkanes, the relative intensity between the two C-H peaks (287-288 eV) was changed when the polarization was directed along the Y direction (right) relative to when the polarization was directed along X direction (left). When the polarization is directed along Y direction (right), the relative intensity of the first C-H peak was

higher than the second C-H peak, and when the polarization is directed along X direction (left), the relative intensity of the first C-H peak was lower than the second C-H peak.

The corresponding calibrated energy for the two C-H transitions (287-288 eV) along the X and Y directions in all four *n*-alkanes and the relative intensity of the two C-H peaks in those two directions are presented in **Table 3.2**.

Table 3.2 Calibrated C-H transition energies of *n*-alkanes when the carbon 1s NEXAFS spectra are recorded with X-ray polarization directed along the X (long axis) and Y (short axis) directions of the crystal.

Type of *n*-alkane		First C-H peak (eV)	Second C-H peak (eV)	Relative intensity between two C-H peaks
$C_{23}H_{48}$ *n*-tricosane	X	287.55	288.15	$1^{st}<2^{nd}$ C-H peak
	Y	287.55	288.04	$1^{st}>2^{nd}$ C-H peak
$C_{24}H_{50}$ *n*-tetracosane	X	287.55	288.04	$1^{st}<2^{nd}$ C-H peak
	Y	287.55	288.06	$1^{st}>2^{nd}$ C-H peak
$C_{28}H_{58}$ *n*-octacosane	X	287.65	288.25	$1^{st}<2^{nd}$ C-H peak
	Y	287.55	288.15	$1^{st}>2^{nd}$ C-H peak
$C_{40}H_{82}$ *n*-tetracontane	X	287.55	288.15	$1^{st}<2^{nd}$ C-H peak
	Y	287.45	287.95	$1^{st}>2^{nd}$ C-H peak

All the energies included in the **Table 3.2** were calibrated with CO_2 (see §2.4.3.2). Furthermore the energies of the two C-H peaks (287-288 eV) along the Y and X axis of the *n*-alkane crystal varied in all four *n*-alkanes. A discussion of the relative reliability of the energy scale follows in §3.3.2.1.

In order to identify the changes in the carbon 1s NEXAFS spectra due to the different intermolecular interactions or crystal packing of *n*-alkanes, the intensity variation between the two C-H peaks in the *n*-alkanes was calculated. This is shown in **Figure 3.12** and **Table 3.3**.

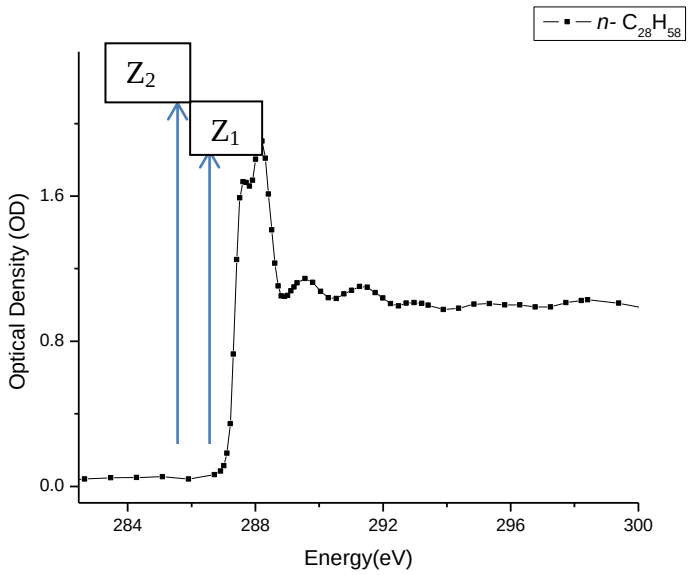

Figure 3.12 Relationship between the intensity of the two carbon 1s → $\sigma^*_{C\text{-}H}$ transitions with respect to highest peak.

The change in the intensity of the two peaks with respect to the highest peak was obtained from the following formula.

$$X = ((Z_1 - Z_2)/ (Z_2)) \times 100 \qquad (3.1)$$

The calibrated intensity values obtained for each *n*-alkane when the spectra was recorded with the X-ray polarization directed along the X (long axis) or along the Y (short axis) direction of the crystal are given in **Table 3.3**.

Table 3.3 Calibrated intensity values obtained from equation 3.1 for the C-H transitions when the spectra are recorded with the X-ray polarization directed along the X (long axis) or along the Y (short axis) direction of the crystal.

Type of *n*-alkane		First C-H peak (Z_1)	Second C-H peak (Z_2)	X=((Z_1-Z_2)/(highest peak))× 100
$C_{23}H_{48}$ *n*-tricosane	X	1.99	2.02	1.5 %
	Y	2.23	2.15	3.6 %
$C_{24}H_{50}$ *n*-tetracosane	X	1.41	1.50	6.0 %
	Y	1.43	1.68	14.9 %
$C_{28}H_{58}$ *n*-octacosane	X	1.01	1.21	16.5 %
	Y	1.26	1.05	16.7 %
$C_{40}H_{82}$ *n*-tetracontane	X	1.07	1.16	7.8 %
	Y	1.13	0.93	17.7 %

According to **Table 3.3**, in all four *n*-alkanes, the intensity change between the two carbon C-H peaks with respect to the highest intensity C-H peak increased when the spectra were recorded with the X-ray polarization directed along the Y direction of the crystals. Also, significantly higher relative intensity values were obtained in *n*-octacosane ($C_{28}H_{58}$) for both directions (X and Y) of the crystal.

The experiment was repeated, and showed similar linear dichroism effect (**Figure 3.11)** in data measured along X and Y directions of crystal, for *n*-tricosane ($C_{23}H_{48}$), *n*-tetracosane ($C_{24}H_{50}$) and *n*-tetracontane ($C_{40}H_{82}$). For the spectrum of *n*-octacosane ($C_{28}H_{58}$), the relative intensity

values observed in repeat was not exactly same as in **Table 3.3.** The difference between the two data sets is a ~10%. However, the trend remains consistent in the two sets of data.

3.3.2.1 Stability of the Monochromator Energy Scale

The monochromator energy scale was unstable with time, and varied from day to day. In order to get a reliable energy scale, the energy scale was calibrated with CO_2 gas (see §2.4.3.2). Two peaks (carbon 1s $\rightarrow$ 3s (292.74 eV) and carbon 1s $\rightarrow \pi^*$ (290.74 eV) transition) were observed in the CO_2 gas spectrum (**Figure 2.16)**. The spectra of *n*-tricosane ($C_{23}H_{48}$), *n*-tetracosane ($C_{24}H_{50}$) and *n*-octacosane ($C_{28}H_{58}$) were taken in the same day. However, due to limited time period in the beamtime, spectrum of *n*-tetracontane ($C_{40}H_{82}$) was obtained in another day. A difference in the energy scale reliability was observed between two different days due to the instability of the energy scale with time, even with the calibration. There is relatively less uncertainty in the energy scale for *n*-tricosane ($C_{23}H_{48}$), *n*-tetracosane ($C_{24}H_{50}$) and *n*-octacosane ($C_{28}H_{58}$) as these were recorded on the same day.

Discussion

Figure 3.11 and **Table 3.2** shows that, for all four *n*-alkanes, the change observed in the relative intensity between the two C-H peaks was the same for the two polarization directions relative to the *n*-alkane crystal (X and Y). When the polarization was directed along the Y direction (**Figure 3.11** right), the relative intensity of the first C-H peak was higher than the second C-H peak and when the polarization is directed along X direction (left), the relative intensity of the first C-H peak was lower than the second C-H peak. This is a clear linear dichroism effect, reflecting different projections of the X-ray polarization on the alkane molecules in the unit cell.

The spectra of *n*-tricosane ($C_{23}H_{48}$), *n*-tetracosane ($C_{24}H_{50}$) and *n*-tetracontane ($C_{40}H_{82}$) are very similar to each other while *n*-octacosane ($C_{28}H_{58}$) was quite different. **Table 3.3** showed that higher relative intensity values were obtained from the equation 3.1 for *n*-octacosane ($C_{28}H_{58}$) along both directions of the crystal (X and Y) with respect to the other *n*-alkanes. *N*-octacosane ($C_{28}H_{58}$) has a monoclinic unit cell, while *n*-tricosane ($C_{23}H_{48}$) and *n*-tetracontane ($C_{40}H_{82}$) are orthorhombic and *n*-tetracosane ($C_{24}H_{50}$) is triclinic. The chains of monoclinic crystals are tilted with respect to the end group plane (see §1.3.1.1) and hence it makes an angle of about 61° with respect to the end group plane.[32,33] This makes a two carbon-carbon unit displacement of *n*-octacosane ($C_{28}H_{58}$) adjacent chains along their axes in monoclinic crystal structure.[32,33] Hence the crystal packing in *n*-octacosane ($C_{28}H_{58}$) appeared to be sufficiently different from the other *n*-alkane species, leading to a change in intermolecular interactions, and thus the differences in the X-ray absorption spectra.

The energy calibration difference could be responsible for some of the spectral differences, but the *n*-octacosane ($C_{28}H_{58}$) data was recorded in the same day as the *n*-tricosane ($C_{23}H_{48}$) and *n*-tetracosane ($C_{24}H_{50}$) spectra, and therefore the energy scale is considered to be more reliable.

3.3 NEXAFS Spectra of *n*-Alkane with Different Crystal Structures through Order-Disorder Transitions

A key development required in this work was the refinement of the heating cell for improved temperature accuracy and stability, for use in measuring the spectra of *n*-alkanes through the solid-solid order-disorder phase transitions. The development of the heating cell was discussed in §2.3.

In this experiment, the *n*-alkane sample was heated up to its melting point. While heating the sample, NEXAFS spectra were obtained at specific temperatures (± 0.2°C) corresponding to specific phases (see **Table 1.1** in §1.3.2.1). Helium gas acts as a cooling agent during the heating process and helium convection prevents the system to reaching a temperature above 60.0 °C. Therefore, all the calibrated spectra were taken under vacuum conditions (< 200 mTorr), in the absence of helium gas. The energy scale calibration procedure was explained in §2.4.3.2.

3.3.1 Carbon 1s NEXAFS Spectra Obtained with Left Circular Polarization

In order to get the quality spectra with minimum radiation damage, the experimental conditions of the NEXAFS spectra were optimized, as discussed in §2.4.3.1 and §2.4.3.2. Furthermore crystals with the same orientation with respect to the X-ray polarization were used during the whole temperature range up to its melting point.

In general, shorter chain *n*-alkanes such as of *n*-tricosane ($C_{23}H_{48}$), *n*-tetracosane ($C_{24}H_{50}$), *n*-octacosane ($C_{28}H_{58}$) were more radiation sensitive than the long chain *n*-tetracontane ($C_{40}H_{82}$).[33] The shorter chain size and higher vapour pressure of the short chain *n*-alkanes makes them more sensitive to mass loss due to radiation. Also the impact of radiation damage increases with temperature.

Changes observed in NEXAFS spectra of *n*-alkanes with different crystal structures which varied by the temperature (order-disorder transitions) were started with shorter chain *n*-alkanes such as *n*-tricosane ($C_{23}H_{48}$), *n*-tetracosane ($C_{24}H_{50}$) and *n*-octacosane ($C_{28}H_{58}$). The apparent rate of mass loss was accelerated for the shorter chain *n*-alkanes, and shorter chain *n*-alkanes evaporated before their order-disorder transition temperatures under the vacuum environment (< 200mTorr). This is shown in **Figure 3.13**.

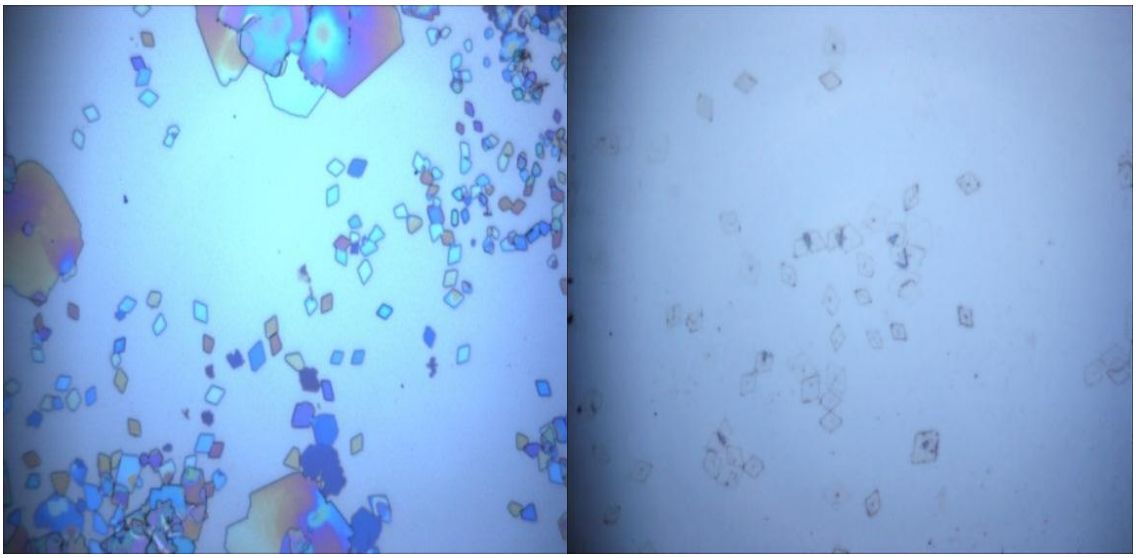

Figure 3.13 Polarized optical microscope images in the *n*-tricosane ($C_{23}H_{48}$) (left) at room temperature (25.4 °C) and (right) at 38.4 °C (50X objective magnification).

N-tricosane ($C_{23}H_{48}$) crystals evaporated at 38.4 °C (± 0.2 °C), below the order-disorder transition temperature of *n*-tricosane ($C_{23}H_{48}$) (see **Table 1.1** in §1.3.2.1). The same observation was observed for *n*-tetracosane ($C_{24}H_{50}$) and *n*-octacosane ($C_{28}H_{58}$). Hence, it was not possible to identify the changes observed in carbon 1s NEXAFS spectroscopy of those shorter chain *n*-alkanes in the order-disorder transitions. This was further confirmed by *in situ* STXM images of *n*-tricosane ($C_{23}H_{48}$) taken in different temperatures at 300 eV.

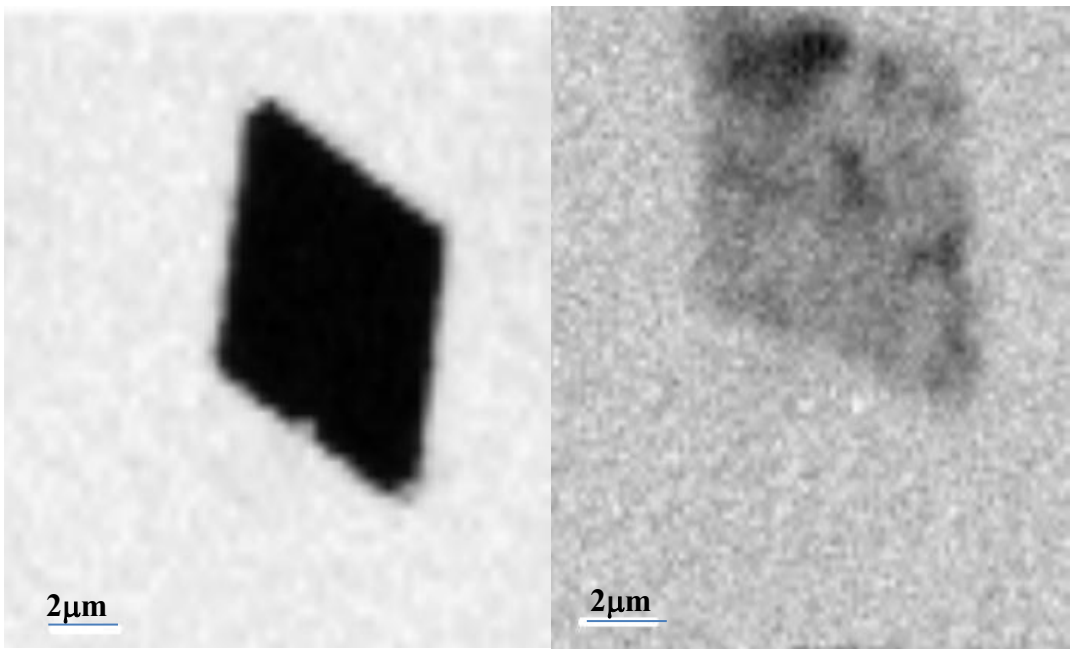

Figure 3.14 STXM images of *n*-tricosane ($C_{23}H_{48}$) at (left) room temperature (25.4 °C) and (right) at 38.4 °C (300 eV)

Figure 3.14 shows the loss of contrast in the STXM image of *n*-tricosane ($C_{23}H_{48}$) at 38.4 °C (± 0.2 °C). This loss of contrast in the STXM image at higher temperature represents mass loss.

As a next step, NEXAFS spectra of *n*-tetracontane ($C_{40}H_{82}$) were obtained as a function of temperature. This sample is more stable with temperature. The spectra variation with in the temperature range is shown in **Figure 3.15**.

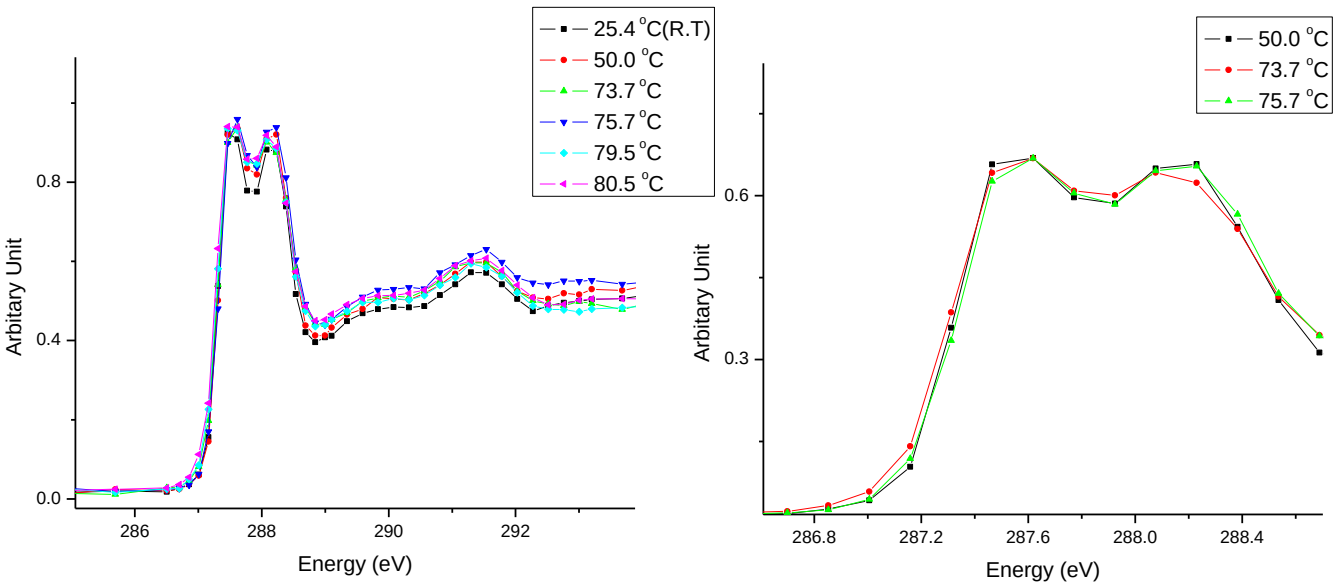

Figure 3.15 Temperature dependent calibrated carbon 1s NEXAFS study of *n*-tetracontane ($C_{40}H_{82}$) (rescaled) recorded with left circularly polarized X-rays.

Figure 3.15 and **Table 3.4** show that spectra are similar to each other, but in the temperature range from 73.7 °C (± 0.2 °C) and 75.8 °C (± 0.2 °C), the relative intensity of the C-H transitions (per equation 3.1) changes slightly. Other than that, no variation was found in the carbon 1s NEXAFS spectra of *n*-tetracontane ($C_{40}H_{82}$) with temperature.

Table 3.4 Calibrated relative intensity values of C-H transitions in *n*-tetracontane ($C_{40}H_{82}$) with changes in temperature.

Temperature	Relative intensity of the two C-H peaks	Relative intensity per equation 3.1
25.4 °C (R.T.)	$1^{st}>2^{nd}$	2.74%
50.0 °C	$1^{st}>2^{nd}$	4.76%
73.7 °C	$1^{st}>2^{nd}$	6.22%
75.8 °C	$1^{st}>2^{nd}$	5.64%
79.5 °C	$1^{st}>2^{nd}$	4.54%
80.5 °C	$1^{st}>2^{nd}$	3.85%

The carbon 1s NEXAFS spectra change observed in the 73.0 °C - 75.0 °C temperature region was further examined by comparing the carbon 1s NEXAFS spectra of *n*-tetracontane ($C_{40}H_{82}$) under different experimental conditions (**Figure 3.16**).

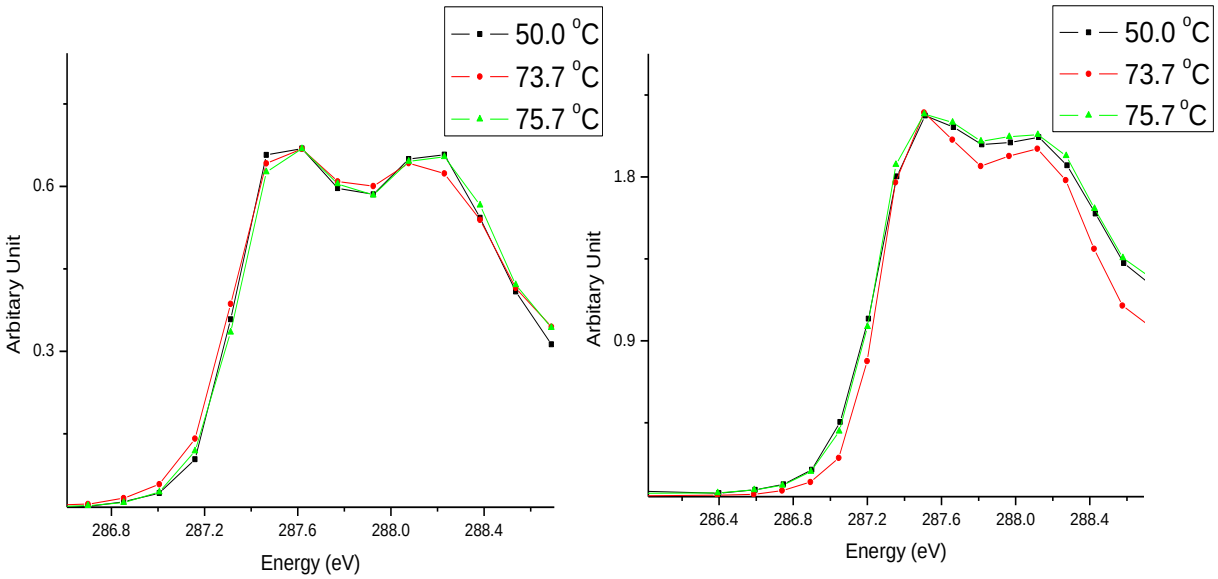

Figure 3.16 Temperature dependent calibrated carbon 1s NEXAFS study of *n*-tetracontane ($C_{40}H_{82}$) (rescaled) recorded with (left) left circular polarization and (Right) linear incline polarization.

In **Figure 3.16** (left), the spectra were obtained with the left circular polarization and **Figure 3.16** (right), the spectra were obtained with inclined linearly polarization. Furthermore, the energy resolutions of the two different experiments were different. The spectra in the **Figure 3.16** (left) have a higher energy resolution (smaller slit size, 13×13 microns) than in **Figure 3.16** (right) (larger slit size, 30×30 microns).

However, the trend observed in the carbon 1s NEXAFS spectra of *n*-tetracontane ($C_{40}H_{82}$) in the temperature range of 73.0 °C - 75.0 °C is the same. In both data sets, the intensity of the second peak decreased at 73.7 °C (± 0.2 °C) and at 75.7 °C (± 0.2 °C), the intensity of the second peak again increased and is close to the relative intensity of the second peak at 50.0 °C (± 0.2 °C) temperature. Therefore, there is a change in the disordered phase (73.0 °C - 75.0 °C) and that change remains consistent in experiments performed with different X-ray polarization.

3.4.1.2 Temperature Instability and Inhomogeneity in the Heating Cell

Even though heating cell worked well with an adequate temperature accuracy and stability in the air and vacuum, instability in the temperature was observed inside the STXM while obtaining the carbon 1s NEXAFS spectra of *n*-alkanes at higher temperatures. The temperature was highly unstable and inaccurate above 80.0 °C.

Figure 3.17 shows how this heating cell worked well under vacuum up to the melting point of *n*-tetracontane ($C_{40}H_{82}$).

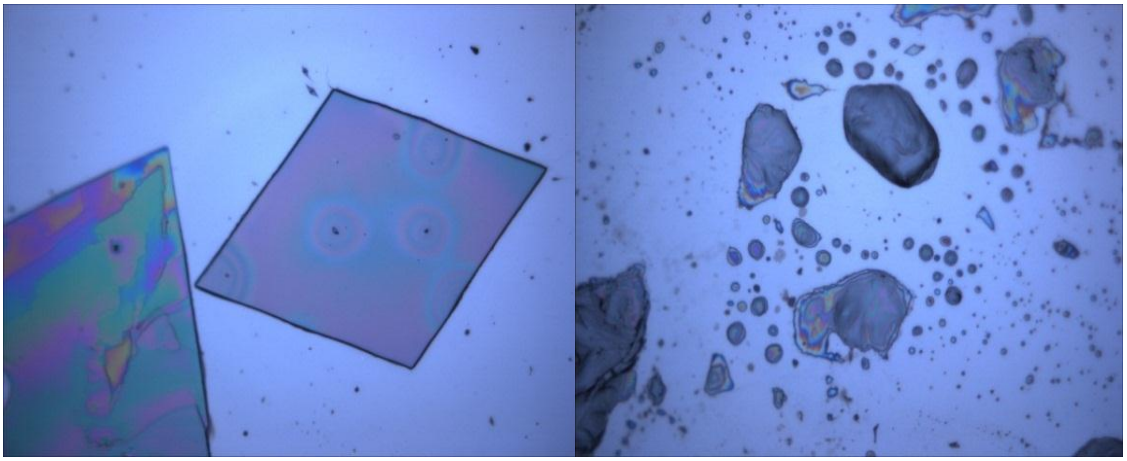

Figure 3.17 Polarized optical microscope images of *n*-tetracontane at (left) room temperature (25.4 °C) and (right) at 82.6 °C (50X objective magnification).

Figure 3.17 shows a sample that was heated inside the STXM up to the temperature 82.6 °C with the X-ray beam off and the image was taken by the polarized optical microscope under bright field illumination when it cooled down back to room temperature (**Figure 3.17** right). Also, under air, it was melted close to the 82.6 °C (± 1 °C) as well.

However *n*-tetracontane ($C_{40}H_{82}$) did not melt in that particular temperature when obtaining carbon 1s NEXAFS spectra of that *n*-alkane inside the STXM with the X-ray beam on. Further, it was found in that particular condition, instability in the temperature was observed beyond 80.0 °C. Inhomogeneous heat distribution was also observed throughout the sample in this experimental condition. In general, Si_3N_4 windows do not have good heat conductivity. Therefore, it was assumed the observed drawbacks (> 80 °C) are due to the poor heat conductivity of the Si_3N_4 window. Hence it is necessary to use better heat conductive substrate in order to obtain good heat distribution and stability in the temperature throughout the sample. This is planned for future work.

Discussion

Short chain *n*-alkanes, *n*-tricosane ($C_{23}H_{48}$), *n*-tetracosane ($C_{24}H_{50}$) and *n*-octacosane ($C_{28}H_{58}$) evaporated before their order-disorder transition temperatures. No changes were observed in the carbon 1s NEXAFS spectra of *n*-tricosane ($C_{23}H_{48}$), *n*-tetracosane ($C_{24}H_{50}$) and *n*-octacosane ($C_{28}H_{58}$) before they sublimed.

In *n*-tetracontane ($C_{40}H_{82}$), the carbon 1s NEXAFS spectra remains almost same except in the temperature range of 73.0 - 75.0 °C (**Figure 3.15** and **Table 3.4**). The change observed in this disordered phase (73.0 - 75.0 °C) remains same with different experimental conditions of the NEXAFS spectroscopy (**Figure 3.16**). The phase transition of *n*-tetracontane ($C_{40}H_{82}$) occurs in this temperature range.

The phase transition was confirmed by polarized optical microscopy images obtained in this temperature range (**Figure 3.7c, d, e**) that show that the morphology of the *n*-tetracontane crystal changed in this temperature range. Secondly, for this particular *n*-alkane; a sharp peak was observed by DSC in this temperature range (**Table 2.1**). Furthermore, this phase transition in this temperature range was confirmed by the literature. Wang *et al.*[40] observed the solid-solid transition of the *n*-tetracontane ($C_{40}H_{82}$) crystal at 74.55 °C (**Table 1.1** and **2.1**), and labeled this as a transition from a M phase (low temperature phase or mesophase) to the C phase (intermediate form between crystalline phase and liquid phase).[40] Therefore, changes in the carbon 1s NEXAFS spectra of *n*-tetracontane ($C_{40}H_{82}$) are believed to be attributed to the phase changes in the *n*-tetracontane ($C_{40}H_{82}$) crystal.

4. Conclusions

Effect of intermolecular interactions on the carbon 1s NEXAFS spectroscopy of *n*-alkanes has been studied for the selected *n*-alkanes such as *n*-tricosane ($C_{23}H_{48}$), *n*-tetracosane ($C_{24}H_{50}$), *n*-octacosane ($C_{28}H_{58}$) and *n*-tetracontane ($C_{40}H_{82}$). Well-ordered diamond shape *n*-alkane single crystals were obtained by using a solution casting method with experimental conditions optimized for each *n*-alkane. The shape of the short chain *n*-alkane crystals such as *n*-tricosane ($C_{23}H_{48}$) and *n*-tetracosane ($C_{24}H_{50}$) were highly ordered at low crystallization temperatures.

The analysis of the carbon 1s NEXAFS spectra of *n*-alkanes recorded with left circularly polarized radiation, at room temperature, showed that linear dichroism is still observed in the spectra even with circularly polarized X-rays. Hence it was concluded significant linear polarization contamination was present in this energy range.

Further, analysis of the angle dependent carbon 1s NEXAFS spectra by aligning the X-ray linear polarization along the principal axes (X, Y) of the crystal reveals that there was a clear linear dichroism effect, reflecting different projections of the X-ray polarization on the alkane molecules in the unit cell. Also the crystal packing in *n*-octacosane ($C_{28}H_{58}$) was sufficiently different than the other *n*-alkane species, leading to a change in intermolecular interactions and the NEXAFS spectra.

The analysis of the temperature dependent carbon 1s NEXAFS studies of *n*-alkanes reveals that the short chain *n*-alkane crystals such as *n*-tricosane ($C_{23}H_{48}$), *n*-tetracosane ($C_{24}H_{50}$) and *n*-octacosane ($C_{28}H_{58}$) evaporated before their order-disorder transitions. However *n*-tetracontane ($C_{40}H_{82}$) crystal shows a NEXAFS spectral change in the phase transition region in the temperature range of 73.0 - 75.0 °C. Hence, the crystal packing of the *n*-tetracontane ($C_{40}H_{82}$) at

that particular temperature range (73.0 - 75.0 °C) was sufficiently different than the other temperature values, leading to a change in intermolecular interactions in the *n*-tetracontane ($C_{40}H_{82}$) and also a change to its NEXAFS spectra. These observations are an example of matrix effects. The interpretations of these effects are difficult and will be a subject for future work. Furthermore it was noted that stability and the heat distribution throughout the sample was not homogeneous at higher temperatures.

5. Future Work

As mentioned in §3.4.1.2, the reason for the fluctuation and instability of the temperature reading above 80.0 °C was hypothesized to be the inhomogeneous heat distribution throughout the substrate. Therefore, the heat conductivity of the substrate material may play an important role. Heat conductivity varied from material to material. This is a measure of a substances ability to transfer heat through a solid by conduction. In general, materials which have high heat conductivity act as heat sinks and materials which have low values act as heat insulators.

The Si_3N_4 window has low heat conductivity compared to other metals such as aluminum and copper. Therefore, in future work, the substrate (100 nm Si_3N_4 window) could be coated with a thin layer of metal with high heat conductivity. Copper may be a good selection as it has high heat conductivity (~ 399.80 W/m.K). The ideal thickness of the copper film can be identified by preparing set of substrate with a different thickness of thin layer of copper (5 nm, 10nm, 15 nm, 20 nm, etc.). Then, temperature measurements of the substrate inside the STXM at higher temperatures will allow to identify the suitable substrate and copper film combination which will show a stable temperature reading with minimum fluctuation. This will allow one to obtain accurate carbon 1s NEXAFS spectra of *n*-alkanes at higher temperatures (above 80.0 °C).

Furthermore, as X-rays produced from the EPU are directed into the plane of grating monochromator, and to the STXM by mirror, linear polarization contamination in this energy range may arise presumably due to the contamination of the beam with the carbon deposition on the mirror. Therefore cleaner optics will minimize the linear dichroism contamination in this energy range.

References

(1) Ade, H.; Urquhart, S. G. In *Chemical Applications of Synchrotron Radiation*; Sharm, T. K., Ed.; World Scientific Publishing: River Edge, NJ, USA, 2002.

(2) Polzonette, G. *Advances in Macromolecules*; Springer Link: Berlin, Germany, 2010.

(3) Prange, A.; Modrow, H. *Reviews in Environmental Science and Biotechnology* **2002,** *1*, 259-276.

(4) Stöhr, J. *NEXAFS Spectroscopy*; Springer-Verlag: Berlin, Germany 1992.

(5) Hähner, G. *Chemical Society Reviews* **2006,** *35*, 1244-1255.

(6) Chen, J. G. *Surface Science Reports* **1997,** *30*, 1-152.

(7) Watts, B.; Thomsen, L.; Dastoor, P. C. *Journal of Electron Spectroscopy and Related Phenomena* **2006,** *151*, 105-120.

(8) Urquhart, S. G.; Hitchcock, A. P.; Smith, A. P.; Ade, H.; Rightor, E. G. *Journal of Physical Chemistry B* **1997,** *101*, 2267-2276.

(9) Fu, J. PhD thesis, University of Saskatchewan, Saskatoon, SK, Canada, 2006.

(10) Fu, J.; Urquhart, S. G. *Journal of Physical Chemistry A* **2005,** *109*, 11724-11732.

(11) Fu, J.; Urquhart, S. G. *Langmuir* **2007,** *23*, 2615-2622.

(12) Thomsen, A. *X-ray Data booklet*; U. S. Government Printing Office: Berkeley, USA, 2009.

(13) Urquhart, S. G.; Gillies, R. *The Journal of Chemical Physics* **2006,** *124*, 234704-8.

(14) Schöll, A.; Fink, R.; Umbach, E.; Mitchell, G. E.; Urquhart, S. G.; Ade, H. *Chemical Physics Letters* **2003,** *370*, 834-841.

(15) Hitchcock, A. P.; Newbury, D. C.; Ishii, I.; Stöhr, J.; Horsley, J. A.; Redwing, R. D.; Johnson, A. L.; Sette, F. *Journal of Chemical Physics* **1986,** *85*, 4849-4862.

(16) Flesch, R.; Pavlychev, A. A.; Neville, J. J.; Blumberg, J.; Kuhlmann, M.; Tappe, W.; Senf, F.; Schwarzkopf, O.; Hitchcock, A. P.; Ruhl, E. *Physical Review Letters* **2001,** *86*, 3767-3770.

(17) Gordon, M. L.; Cooper, G.; Morin, C.; Araki, T.; Turci, C. C.; Kaznatcheev, K.; Hitchcock, A. P. *Journal of Physical Chemistry A* **2003,** *107*, 6144-6159.

(18) Pettersson, L. G. M.; Nilsson, A.; Myneni, S.; Luo, Y.; Nyberg, M.; Cavalleri, M.; Ojamae, L.; Naslund, L. A.; Ogasawara, H.; Odelius, M.; Pelmenschikov, A. *Journal of Synchrotron Radiation* **2001,** *8*, 136-140.

(19) Ishii, I.; Hitchcock, A. P. *Journal of Electron Spectroscopy and Related Phenomena* **1988,** *46*, 55-84.

(20) Schöll, A.; Zou, Y.; Kilian, L.; Hubner, D.; Gador, D.; Jung, C.; Urquhart, S. G.; Schmidt, T.; Fink, R.; Umbach, E. *Physical Review Letters* **2004,** *93*, 1464061-1464064.

(21) Ma, Y.; Chen, C. T.; Meigs, G.; Randall, K.; Sette, F. *Physical Review A* **1991,** *44*, 1848-1858.

(22) Remmers, G.; Domke, M.; Kaindl, G. *Physical Review A* **1993,** *47*, 3085-3091.

(23) Ueda, K.; Okunishi, M.; Chiba, H.; Shimizu, Y.; Ohmori, K.; Sato, Y.; Shigemasa, E.; Kosugi, N. *Chemical Physics Letters* **1995,** *236*, 311-317.

(24) Schirmer, J.; Trofimov, A. B.; Randall, K. J.; Feldhaus, J.; Bradshaw, A. M.; Ma, Y.; Chen, C. T.; Sette, F. *Physical Review A* **1993,** *47*, 1136-1147.

(25) Stöhr, J.; Outka, D. A.; Baberschke, K.; Arvanitis, D.; Horsley, J. A. *Physical Review B* **1987,** *36*, 2976-2979.

(26) Outka, D. A.; Stohr, J.; Rabe, J. P.; Swalen, J. D.; Rotermund, H. H. *Physical Review Letters* **1987,** *59*, 1321-1324.

(27) Bagus, P. S.; Weiss, K.; Schertel, A.; Wöll, C.; Braun, W.; Hellwig, C.; Jung, C. *Chemical Physics Letters* **1996,** *248*, 129-135.

(28) Weiss, K.; Bagus, P. S.; Wöll, C. *Journal of Chemical Physics* **1999,** *111*, 6834-6845.

(29) Weiss, K.; Ostrom, H.; Triguero, L.; Ogasawara, H.; Garnier, M. G.; Pettersson, L. G. M.; Nilsson, A. *Journal of Electron Spectroscopy and Related Phenomena* **2003,** *128*, 179-191.

(30) Vaterlein, P.; Fink, R.; Umbach, E.; Wurth, W. *Journal of Chemical Physics* **1998,** *108*, 3313-3320.

(31) Urquhart, S. G.; Gillies, R. *Journal of Physical Chemistry A* **2005,** *109*, 2151-2159.

(32) Turner, W. R. *Product R&D* **1971,** *10*, 238-260.

(33) Kawaguchi, A. *Bulletin of the Institute for Chemical Research* **1981,** *59*, 284-292.

(34) Chazhengina, S. Y.; Kotelnikova, E. N.; Filippova, I. V.; Filatov, S. K. *Journal of Molecular Structure* **2003,** *647*, 243-257.

(35) Doucet, J.; Denicolo, I.; Craievich, A.; Collet, A. *Journal of Chemical Physics* **1981,** *75*, 5125-5127.

(36) Sirota, E. B.; Singer, D. M. *Journal of Chemical Physics* **1994,** *101*, 10873-10882.

(37) Chevallier, V.; Bouroukba, M.; Petitjean, D.; Barth, D.; Dupuis, P.; Dirand, M. *Journal of Chemical and Engineering Data* **2001,** *46*, 1114-1122.

(38) Kraack, H.; Sirota, E. B.; Deutsch, M. *Journal of Chemical Physics* **2000,** *112*, 6873-6885.

(39) Kotelnikova, E. N.; Filippova, I. V.; Filatov, S. K. *Journal of Structural Chemistry* **1995,** *36*, 718-724.

(40) Wang, S. L.; Tozaki, K. I.; Hayashi, H.; Inaba, H.; Yamamoto, H. *Thermochimica Acta* **2006,** *448*, 73-81.

(41) Zou, Y.; Araki, T.; Appel, G.; Kilcoyne, A. L. D.; Ade, H. *Chemical Physics Letters* **2006,** *430*, 287-292.

(42) Dirand, M.; Bouroukba, M.; Briard, A. J.; Chevallier, V.; Petitjean, D.; Corriou, J. P. *Journal of Chemical Thermodynamics* **2002,** *34*, 1255-1277.

(43) Nozaki, K.; Higashitani, N.; Yamamoto, T.; Hara, T. *Journal of Chemical Physics* **1995,** *103*, 5762-5766.

(44) Denicolo, I. *Journal of Chemical Physics* **1981,** *80*, 1647-1651.

(45) Yamamoto, Y.; Mitsumoto, R.; Ito, E.; Araki, T.; Ouchi, Y.; Seki, K.; Takanishi, Y. *Journal of Electron Spectroscopy and Related Phenomena* **1996,** *78*, 367-370.

(46) Murphy, D. B.; Davidson, M. W. *Fundamentals of Light Microscopy and Electronic Imaging*; Wiley Blackwell: New York, USA, 2001.

(47) Nikon introduction to the polarized optical microscopy page.
http://www.microscopyu.com/articles/polarized/polarizedintro.html (accessed on Sep 2012).

(48) Wikipedia polarization page.
http://en.wikipedia.org/wiki/Polarization_%28waves%29 (accessed on Sep 2012).

(49) Kitamura, H. *Journal of Synchrotron Radiation* **2000,** *7*, 121-130.

(50) Otero, E. PhD thesis, University of Saskatchewan, Saskatoon, SK, Canada, 2008.

(51) Hitchcock, A. P.; Dynes, J. J.; Johansson, G. R.; Wang, J.; Botton, G. *Micron* **2008,** *39*, 311-319.

(52) Stöhr, J. *Surface Review & Letters* **1998,** *5*, 1297-1308.

(53) Graf-Zeiler, B.; Fink, R. H.; Tzvetkov, G. *Journal of Physical Chemistry and Chemical Physics* **2011,** *12*, 3503-3509.

(54) Jacobson, C. *Journal of Microscopy* **2000,** *197*, 173-184.

(55) *aXis 2000*; software for analysis of X-ray microscopy images and spectra; McMaster University: Ontario, Canada, 2000.

(56) *Origin*; version 7.5; software for data analysis and graphing; Origin Lab: Northampton State, USA, 1991.